Monthly Notices
of the
ROYAL ASTRONOMICAL SOCIETY

MNRAS **460,** 3255–3271 (2016)
Advance Access publication 2016 May 23

doi:10.1093/mnras/stw1227

Dynamical mass ejection from binary neutron star mergers

David Radice,[1]★ Filippo Galeazzi,[2] Jonas Lippuner,[1] Luke F. Roberts,[1]†
Christian D. Ott[1] and Luciano Rezzolla[2,3]

[1]*TAPIR, Walter Burke Institute for Theoretical Physics, MC 350-17, California Institute of Technology, Pasadena, CA 91125, USA*
[2]*Institute for Theoretical Physics, Max-von-Laue Str. 1, D-60438 Frankfurt, Germany*
[3]*Frankfurt Institute for Advanced Studies, Ruth-Moufang-Str. 1, D-60438 Frankfurt Germany*

Accepted 2016 May 18. Received 2016 May 18; in original form 2016 January 11

ABSTRACT

We present fully general-relativistic simulations of binary neutron star mergers with a temperature and composition dependent nuclear equation of state. We study the dynamical mass ejection from both quasi-circular and dynamical-capture eccentric mergers. We systematically vary the level of our treatment of the microphysics to isolate the effects of neutrino cooling and heating and we compute the nucleosynthetic yields of the ejecta. We find that eccentric binaries can eject significantly more material than quasi-circular binaries and generate bright infrared and radio emission. In all our simulations the outflow is composed of a combination of tidally- and shock-driven ejecta, mostly distributed over a broad $\sim 60^\circ$ angle from the orbital plane, and, to a lesser extent, by thermally driven winds at high latitudes. Ejecta from eccentric mergers are typically more neutron rich than those of quasi-circular mergers. We find neutrino cooling and heating to affect, quantitatively and qualitatively, composition, morphology, and total mass of the outflows. This is also reflected in the infrared and radio signatures of the binary. The final nucleosynthetic yields of the ejecta are robust and insensitive to input physics or merger type in the regions of the second and third r-process peaks. The yields for elements on the first peak vary between our simulations, but none of our models is able to explain the Solar abundances of first-peak elements without invoking additional first-peak contributions from either neutrino and viscously-driven winds operating on longer time-scales after the mergers, or from core-collapse supernovae.

Key words: gravitational waves – hydrodynamics – neutrinos – nuclear reactions, nucleosynthesis, abundances – methods: numerical – stars: neutron.

1 INTRODUCTION

Binary neutron star (BNS) and black hole neutron-star (BHNS) mergers can result in the dynamical ejection of neutron star (NS) matter due to tidal torques and/or, in the binary neutron stars (BNS) case, shocks during the merger. This neutron-rich material has long been proposed as a possible origin for the elements with atomic mass number $A \gtrsim 120$ (Lattimer & Schramm 1974; Eichler et al. 1989; Meyer 1989; Freiburghaus, Rosswog & Thielemann 1999). As the ejecta expand and cool they realize the right conditions for the activation of the so-called rapid neutron capture process (*r-process*), synthesizing neutron-rich nuclei.

This scenario has received renewed attention in recent years. On the one hand, detailed calculations have shown that core-collapse supernovae, once considered to be the main candidate for the production of the r-process elements, do not appear to host the right conditions to create the most neutron-rich nuclei (e.g. Fischer et al. 2010; Hüdepohl et al. 2010; Roberts, Woosley & Hoffman 2010). On the other hand, the most recent general-relativistic (GR) simulations of the mass ejection occurring during BNS (Bauswein, Goriely & Janka 2013; Hotokezaka et al. 2013; Wanajo et al. 2014; Foucart et al. 2016; Kastaun & Galeazzi 2015; Palenzuela et al. 2015; Sekiguchi et al. 2015) and black-hole neutron stars (BHNS) (e.g. Foucart et al. 2014; Kyutoku et al. 2015) mergers, as well as in the later evolution of the post-merger remnant (e.g. Dessart et al. 2009; Metzger & Fernández 2014; Fernández et al. 2015b; Foucart et al. 2015; Just et al. 2015; Martin et al. 2015), suggest that mergers are likely to eject a large amount of r-process material (Rosswog et al. 1999; Korobkin et al. 2012; Wanajo et al. 2014; Just et al. 2015; Martin et al. 2015).

In the past, simple models of galactic chemical evolution found issues with the evolution of the r-process abundances under the assumption that compact object binary mergers are the primary source of the r-process. The large amount of material ejected per event

★E-mail: dradice@caltech.edu
† NASA Einstein Fellow.

predicts a larger spread in r-process enrichment of metal poor halo stars than what is observed, when using simple models of galactic chemical evolution (Qian 2000; Argast et al. 2004). Additionally, the delay time between binary formation and merger can result in r-process nucleosynthesis only occurring at somewhat higher metallicity than it is observed to begin at (Argast et al. 2004). In more recent models of galactic chemical evolution performed within cosmological zoom-in simulations (Shen et al. 2015; van de Voort et al. 2015) or by accounting for accretion of sub-haloes into the Milky Way halo (Ishimaru, Wanajo & Prantzos 2015) these problems seem to be mitigated and better agreement with the observed distribution of r-process elements in the Milky Way is found. However, the results of these models are sensitive to numerical resolution and to their treatment of mixing.

On the other hand, the idea that compact binary mergers could be the site of the r-process is also tentatively supported by the recent discovery of an infrared transient associated with *Swift* short gamma-ray burst (SGRB) 130603B (Berger, Fong & Chornock 2013; Tanvir et al. 2013) that might be explained by the radioactive decay of by-products of the r-process in a *macronova* (sometimes also called *kilonova*) (e.g. Li & Paczynski 1998; Kulkarni 2005; Metzger et al. 2010; Roberts et al. 2011; Barnes & Kasen 2013; Kasen, Badnell & Barnes 2013; Tanaka & Hotokezaka 2013; Grossman et al. 2014; Rosswog et al. 2014; Lippuner & Roberts 2015). Other evidence includes the Solar system abundance of ^{244}Pu (Hotokezaka, Piran & Paul 2015; Wallner et al. 2015) and recent observations of r-process enriched stars in a metal-poor ultra-faint dwarf galaxy (Ji et al. 2016). Both of these observations suggest that r-process elements might be preferentially produced in rare/high-yield events such as mergers instead of common/low-yield occurrences such as core-collapse supernovae.

Beside powering macronovae, the outflows from BNS and BHNS mergers could also generate radio flares over time-scales of months to years as their kinetic energy is deposited in the interstellar medium (Nakar & Piran 2011), and could explain the extended X-ray emission observed in some SGRBs (Ciolfi & Siegel 2015; Rezzolla & Kumar 2015). Mergers are also loud gravitational-wave (GW) sources and one of the targets for the nascent field of GW astronomy (Sathyaprakash & Schutz 2009), recently inaugurated with the detection of GWs from a pair of merging black holes (BHs) (Abbott et al. 2016). BNS mergers are promising sources for ground-based laser-interferometer detectors such as Advanced LIGO (LIGO Scientific Collaboration et al. 2015), Advanced Virgo (Acernese et al. 2015), and KAGRA (Aso et al. 2013). Finally, BNS and BHNS mergers are also thought to create the central engines of SGRB (Nakar 2007; Berger 2014; Rosswog 2015). This makes BNS and BHNS mergers ideal candidates for multi-messenger astronomy (Metzger & Berger 2012; Nissanke, Kasliwal & Georgieva 2013) and motivates the systematic study of their observational signatures.

Most previous studies of BNS and BHNS mergers focused on the case of 'primordial' binaries (i.e. formed in an already bound state) which merge under the effect of GW losses at zero eccentricity. However, high-eccentricity mergers might also occur in dense stellar environments such as globular clusters (GCs). About 10 per cent of all observed SGRBs show offsets larger than 20 kiloparsecs from the bulge of their host galaxies (Berger et al. 2005; Berger 2014). In comparison, no long-GRBs have been found with an offset of more than 10 kpc from their host galaxies (Berger 2014). These offsets could be the result of kicks imparted to the binaries at birth, or they could be explained by 10 per cent of SGRB progenitors being located in GCs around their host galaxies (Berger 2014). GCs are dense environments (especially when they undergo the core collapse phase) in which tidal captures, collisions, and dynamically formed binaries from two- or three-body interactions become a more viable channel for BNS and BHNS mergers than in the galactic stellar field (Lee, Ramirez-Ruiz & van de Ven 2010).

Current estimates for the rates of eccentric BNS mergers in GCs are unfortunately plagued by many uncertainties stemming from unknown properties of GCs, such as the number of NSs in the GC core (Murphy, Cohn & Lugger 2011). Recently, Tsang (2013) reviewed the estimates for binary collisions and tidal captures in GC and arrived at a conservative estimate of $0.5\,\mathrm{yr}^{-1}\,\mathrm{Gpc}^{-3}$. However, Tsang (2013) leaves open the possibility that neglected contributions, such as the interaction of a single NS with a binary system or rarer binary–binary interactions, might increase these rates. In any case, even under the most optimistic assumptions, dynamical-capture BNS mergers would account for only a few per cent of the total BNS merger rate.

Nevertheless, eccentric mergers might eject significantly larger amounts of mass than non-eccentric, quasi-circular, mergers (East & Pretorius 2012; Rosswog, Piran & Nakar 2013). As a consequence, they could be contributing an important fraction of the overall r-process element abundances, despite being rarer. For the same reason, eccentric BNS mergers would also give birth to particularly bright electromagnetic (EM) emissions in the infrared and radio bands compared with quasi-circular binaries. Additionally, eccentric BNS mergers produced by dynamical captures in dense stellar environments can potentially produce r-process nuclei at very low metallicity and account for the r-process enhancements seen in some carbon enhanced metal poor stars (Ramirez-Ruiz et al. 2015).

To date, only few GR studies considered eccentric BNS (East & Pretorius 2012; Gold et al. 2012; Paschalidis et al. 2015; East et al. 2016) and BHNS (Stephens, East & Pretorius 2011; East, Pretorius & Stephens 2012a; East, Paschalidis & Pretorius 2015) mergers. Eccentric mergers were also considered in Newtonian physics by Lee et al. (2010) and Rosswog et al. (2013). All of these studies, apart from the Newtonian simulations of Rosswog et al. (2013), employed idealized equations of state. No previous study considered eccentric mergers in full-GR, with a microphysical temperature- and composition-dependent equation of state (EOS), and with the inclusion of neutrino emission and absorptions. GR, microphysical EOS, and neutrinos are three ingredients that are necessary to accurately model the mass ejection and the nucleosynthetic yields from these events. Neutrino transport, in particular, has been recently suggested to have an important role in shaping the composition of the ejecta by Wanajo et al. (2014); Sekiguchi et al. (2015); Foucart et al. (2015, 2016). This, in turn, might affect the nucleosynthetic yields (Wanajo et al. 2014; Goriely et al. 2015) and, possibly, the properties of the macronova emission (Metzger & Fernández 2014; Lippuner & Roberts 2015).

The goal of this paper is to develop a comprehensive understanding of the physics driving dynamical mass ejection in BNS mergers. On the one hand, we quantify the impact of weak reactions and neutrino radiation on the properties of the ejecta, including composition and geometry, extending the works of Wanajo et al. (2014); Sekiguchi et al. (2015); Foucart et al. (2015, 2016). On the other hand, we study, for the first time in full-GR and including a microphysical EOS and neutrino cooling/heating, the mass ejection in eccentric mergers.

Towards these goals we perform a series of full-GR simulations of merging BNS in eccentric and quasi-circular orbits. For the eccentric mergers, we consider *five* possible configurations leading to a variety of different outcomes, including prompt and delayed BH

formation, while all our quasi-circular simulations show delayed BH formation. We systematically vary the level of sophistication of our microphysical description to isolate the effects of local weak reactions (mainly captures on neutrons) and neutrino irradiation from the merger remnant.

The remainder of this paper is organized as follows. We discuss our numerical models, simulation methods, and initial data in Section 2. We present our main results in Section 3, while Section 4 is dedicated to discussion and conclusions. Appendix A describes our treatment of neutrino radiation. Finally, Appendix B contains some non-standard implementation details of the operator split technique we use to treat the weak source/sink terms in the hydrodynamics equations.

Unless otherwise specified, we use a system of units such that $c = G = \mathrm{M}_\odot = 1$, where c is the speed of light in vacuum, G is the gravitational constant, and $\mathrm{M}_\odot$ is the mass of the Sun. We use Einstein's convention of summation over repeated indices. Latin indices run over 1, 2, 3, while Greek indices run over 0, 1, 2, 3. The spacetime metric signature we adopt is $(-, +, +, +)$.

2 NUMERICAL MODEL

2.1 GR hydrodynamics

We simulate the merging NSs using the equations of GR hydrodynamics (e.g. Rezzolla & Zanotti 2013). We evolve the equation of baryon number conservation

$$\nabla_\alpha (n\, u^\alpha) = 0\,, \tag{1}$$

where n is the baryon-number density and u^α is the fluid four-velocity, together with the equations describing conservation of energy and momentum,

$$\nabla_\beta T^{\alpha\beta} = \Psi^\alpha\,. \tag{2}$$

NS matter is treated as a perfect fluid and thus with energy–momentum tensor

$$T^{\alpha\beta} = \rho\, h\, u^\alpha\, u^\beta + p\, g^{\alpha\beta}\,, \tag{3}$$

where ρ is the rest-mass density,

$$\rho = m_b\, n\,, \tag{4}$$

m_b is the fiducial baryon mass, $h = 1 + \epsilon + p/\rho$ is the specific enthalpy, ϵ is the specific internal energy, p is the pressure, and $g^{\alpha\beta}$ is the spacetime metric. Finally, Ψ^α is a source term used to model weak interactions (more on this in Section 2.2).

Equations (1) and (2) are closed by means of an equation of state (EOS) $p = p(n, \epsilon, Y_e)$, where Y_e is the proton (or electron) fraction. For this work we adopt the EOS of Lattimer & Swesty (1991), with nuclear compressibility parameter $K = 220$ MeV. This EOS is broadly consistent with observations, but falls outside the favoured region of microscopic neutron matter calculations (e.g. Fischer et al. 2014). It predicts a maximum non-rotating NS gravitational mass of $2.05\,\mathrm{M}_\odot$ and a $1.4\,\mathrm{M}_\odot$ −NS circumferential radius of 12.8 km.

In some of the simulations we neglect weak interactions and we assume the proton number $n_e = nY_e$ to be conserved. In this case, we also set Ψ^α in equation (2) to zero. In most simulations, however, we do not assume n_e to be conserved, but we evolve the composition taking into account weak interactions,

$$\nabla_\alpha (n_e\, u^\alpha) = R\,, \tag{5}$$

where R is the net lepton number emission/absorption rate per unit volume in the fluid rest-frame. In this case, the energy–momentum source terms read

$$\Psi^\alpha = Q\, u^\alpha\,, \tag{6}$$

where Q is the net neutrino cooling/heating rate per unit volume in the fluid rest-frame. The way we compute R and Q is described in Section 2.2.

Equations (3) and (5) are discretized in flux-conservative form using the WHISKYTHC code (Radice & Rezzolla 2013; Radice, Rezzolla & Galeazzi 2014b, 2015). WHISKYTHC implements both finite-volume and high-order finite-differencing high-resolution shock-capturing methods. For the simulations presented in this work, we use the high-order MP5 primitive reconstruction scheme (Suresh & Huynh 1997) in combination with second order numerical fluxes computed with the HLLE flux formula (Einfeldt 1988). In all simulations we employ the positivity preserving limiter presented in Radice, Rezzolla & Galeazzi (2014a), which minimizes errors related to the numerical density floor.

WHISKYTHC directly evolves the proton n_e and neutron $n - n_e$ number densities thereby guaranteeing the local conservation of both species. In addition, WHISKYTHC also implements a variant of the consistent multi-fluid advection (CMA) method originally proposed by Plewa & Müller (1999). This scheme minimizes advection errors near strong density and compositional gradients, such as at the surface of an NS. We find the use of the CMA scheme to be crucial for quasi-circular binaries that otherwise accumulate significant advection errors close to the surface during their inspiral. On the other hand, the CMA method does not seem to be critical for eccentric binaries. The latter have a relatively short approaching phase and, in the case of models undergoing multiple encounters, generate a dense, well-resolved, 'envelope' after their first encounter (see Section 3.1). For this reason, we employ the CMA scheme only for the quasi-circular binaries. However, we verify the robustness of our results by simulating one of the eccentric models using the CMA scheme.

Finally, we evolve the spacetime with the BSSNOK formulation of the Einstein equations (Nakamura, Oohara & Kojima 1987; Shibata & Nakamura 1995; Baumgarte & Shapiro 1999), using the MCLACHLAN code (Brown et al. 2009), which is part of the EINSTEIN TOOLKIT (Löffler et al. 2012), and a fourth-order accurate finite-difference scheme.

2.2 Neutrino treatment

Our neutrino treatment is based on a so-called grey (energy-averaged) leakage scheme, which is a parametrized neutrino cooling scheme that has been widely used for both core-collapse supernovae and BNS simulations (e.g. van Riper & Lattimer 1981; Ruffert, Janka & Schäfer 1996; Rosswog, Ramirez-Ruiz & Davies 2003; O'Connor & Ott 2010; Perego, Cabezón & Käppeli 2015). Our leakage scheme is an evolution of the scheme presented in Galeazzi et al. (2013). It follows very closely the method used in Ruffert et al. (1996), with the additional simplification that we use the local thermodynamical equilibrium chemical potential for the neutrinos while computing opacities as done in Rosswog et al. (2003). Finally, for the calculation of the optical depth, we adopt the prescription presented in Neilsen et al. (2014), which is well suited for complex geometries as the ones encountered in BNS mergers.

Here, we limit our discussions to the aspects of our leakage scheme that differs from theirs. The basic idea of the leakage scheme is to compute a series of effective emissivities R^{eff} and Q^{eff} for

Table 1. Summary of key results for all models. We report the model name, the (Newtonian) periastron radius r_p, the total ejected mass $M_{\rm ej}$, the mass-averaged proton fraction $\langle Y_e \rangle$, specific entropy per baryon $\langle s \rangle$, and asymptotic velocity of the ejecta, $\langle v_\infty \rangle$, measured on a sphere with coordinate radius $r = 200\,{\rm M}_\odot \simeq 295\,{\rm km}$. We also report the total kinetic energy of the ejecta $E_{\rm kin}$, the macronova peak time $t_{\rm peak}$ (equation 9) luminosity L (equation 10), and effective temperature T (equation 11), as well as the deceleration time of the ejecta $t_{\rm dec}$ (equation 12) and the radio fluence F_ν (i.e. the flux density per unit frequency) during $t_{\rm dec}$ (equation 13). In the case of simulations where we observe BH formation, we also include the remnant torus mass $M_{\rm torus}$ at 1 ms after the formation of the apparent horizon. Simulations with names with prefix LK do not account for neutrino re-absorption, while runs with prefix M0 include neutrino re-absorption using the scheme discussed in Appendix A. Simulations with names prefixed by HY neglect all weak interactions. Names with suffix QC represent models constructed with quasi-circular initial data, while names with suffix RPX represent parabolic models having (Newtonian) periastron radius of $X\,{\rm M}_\odot$.

Model	r_p [km]	$M_{\rm torus}$ [$10^{-2}\,{\rm M}_\odot$]	$M_{\rm ej}$ [$10^{-2}\,{\rm M}_\odot$]	$\langle Y_e \rangle$	$\langle s \rangle$ [k_b]	$\langle v_\infty \rangle$ [$10^{-1}\,c$]	$E_{\rm kin}$ [10^{51} erg]	$t_{\rm peak}$ [d]	L [10^{41} erg s^{-1}]	T [$10^3 K$]	$t_{\rm dec}$ [yr]	F_ν [mJy]
HY_QC[a]	45.00	13.48	0.49	0.04	18.8	1.5	0.125	2.8	0.25	2.4	9.9	0.027
LK_QC[a]	45.00	5.45	0.16	0.15	14.4	1.9	0.065	1.4	0.20	2.8	5.3	0.028
M0_QC[a]	45.00	7.40	0.17	0.17	14.8	1.6	0.053	1.6	0.18	2.8	6.5	0.015
LK_RP0[b]	0.00	0.00	–	–	–	–	–	–	–	–	–	–
HY_RP5	7.38	0.17	0.04	0.05	28.4	4.1	0.078	0.5	0.20	3.3	1.5	0.285
LK_RP5	7.38	0.17	0.02	0.20	17.1	3.3	0.025	0.4	0.14	3.8	1.5	0.051
M0_RP5	7.38	0.16	0.02	0.25	19.8	3.6	0.040	0.4	0.16	3.6	1.5	0.104
HY_RP7.5	11.08	–	7.02	0.04	13.4	2.1	3.681	8.9	0.81	1.5	16.8	2.170
LK_RP7.5_LR[a,c]	11.08	–	2.31	0.14	10.6	1.6	0.687	5.9	0.45	1.8	15.8	0.179
LK_RP7.5	11.08	–	2.67	0.14	10.6	1.7	0.890	6.2	0.49	1.8	15.5	0.274
M0_RP7.5	11.08	–	4.55	0.16	10.5	1.8	1.656	7.8	0.62	1.6	17.2	0.609
HY_RP10	14.78	–	12.54	0.04	9.3	1.5	2.952	14.3	0.78	1.4	29.0	0.628
LK_RP10	14.78	–	5.37	0.09	8.2	1.7	1.812	8.6	0.65	1.6	18.5	0.621
M0_RP10	14.78	–	5.41	0.10	8.3	1.7	1.829	8.6	0.65	1.6	18.5	0.629
LK_RP15[b]	22.15	–	–	–	–	–	–	–	–	–	–	–

Notes. [a]This simulation uses the CMA scheme (see Section 2.1).
[b]The ejected mass for this model is too small to be reliably measured.
[c]This is a low-resolution simulation. Grid spacing on the inner AMR level of $h \simeq 369$ m.

electron neutrinos ν_e, anti-electron neutrinos $\bar{\nu}_e$ and the heavy-lepton neutrinos, which we collectively label as ν_x. These rates are reduced with respect to the intrinsic emissivities in a way that mimics the diffusion of radiation from the high optical depth region. In addition to this, our scheme also estimates heating and lepton-deposition from the absorption of free-streaming neutrinos. The inclusion of neutrino absorption is motivated by the recent works of Wanajo et al. (2014); Sekiguchi et al. (2015); Foucart et al. (2015, 2016), which showed, using grey two-moment schemes (Shibata et al. 2011), that neutrino absorption can alter the composition of the ejecta. The source terms appearing in equations (5) and (6) are then computed as

$$R = (\kappa_{\nu_e} n_{\nu_e} - \kappa_{\bar{\nu}_e} n_{\bar{\nu}_e}) - (R^{\rm eff}_{\nu_e} + R^{\rm eff}_{\bar{\nu}_e}) \tag{7}$$

and

$$Q = (\kappa_{\nu_e} n_{\nu_e} E_{\nu_e} + \kappa_{\bar{\nu}_e} n_{\bar{\nu}_e} E_{\bar{\nu}_e}) - (Q^{\rm eff}_{\nu_e} + Q^{\rm eff}_{\bar{\nu}_e} + Q^{\rm eff}_{\nu_x}), \tag{8}$$

where the κ's are the absorption opacities and n_{ν_e}, $n_{\bar{\nu}_e}$ are the free-streaming neutrino and anti-neutrino number densities in the fluid rest-frame. Finally, E_{ν_e} and $E_{\bar{\nu}_e}$ are the average energies of the free-streaming neutrinos in the fluid rest-frame.

To compute n_{ν_e}, $n_{\bar{\nu}_e}$, E_{ν_e}, and $E_{\bar{\nu}_e}$, we evolve the zeroth moment (M0) of the free-streaming neutrino distribution function on a set of individual radial rays. For that, we use a closure adapted to the post-merger geometry discussed in detail in Appendix A. Our scheme is simpler than the two-moment grey method recently used by Wanajo et al. (2014); Sekiguchi et al. (2015); Foucart et al. (2015, 2016). However, since it tracks both neutrino density and average energies, it allows us to model a number of important effects that cannot be easily incorporated into grey schemes. In particular, our scheme takes gravitational redshift, velocity dependence and non local-thermodynamical equilibrium effects into account, albeit with some major approximations. More details of our radiation transport scheme are given in Appendix A, while some technical details of the coupling with the hydrodynamics are discussed in Appendix B. Note that heating in the M0 code is switched-on only shortly before the merger, because our prescription is not suitable for the phase when the two NSs are still separated and heating is obviously not relevant. After BH formation, we also excise the area inside and close to the apparent horizon in the M0 scheme. In most simulations, with the exception of the M0_QC, we do not excise the hydrodynamic variables, but follow the approaches described in Baiotti & Rezzolla (2006), for the metric evolution, and in Galeazzi et al. (2013), for the EOS and primitive recovery routines.

2.3 Initial data and grid setup

We consider two families of initial data. One describing two NSs on Newtonian parabolic orbits with varying (Newtonian) periastron radius r_p, and another family describing binaries in quasi-circular (low eccentricity) orbits. In both cases, we fix the mass ratio to one (equal mass binaries). A summary of all evolved models is presented in Table 1.

We construct the eccentric initial data using binaries where each star has gravitational mass at infinite separation $M_\infty = 1.389\,{\rm M}_\odot$ and baryonic mass $M_b = 1.522\,{\rm M}_\odot$. We prepare the initial data by superimposing two Tolman-Oppenheimer-Volkoff (TOV) (Tolman 1939; Oppenheimer & Volkoff 1939) solutions in neutrino-less beta equilibrium at the initial separation of $100\,{\rm M}_\odot \simeq 148\,{\rm km}$. We set

the orbital velocity of the two stars according to Newton's law to have a Newtonian periastron radius of 0, 5 $M_\odot$, 7.5 $M_\odot$, 10 $M_\odot$, and 15 $M_\odot$ ($\simeq$0, 7.38 km, 11.08 km, 14.76 km, and 22.15 km).

Since this construction does not yield an exact solution to Einstein equations, it results in violations of the Hamiltonian constraint equations that are between 1 and 2 orders of magnitude larger than for quasi-circular binary initial data. These values are within an acceptable range in that the constraints remain well behaved during the evolution. On the other hand, since we do not solve for the hydrostatic equilibrium of the NSs after boosting them, this triggers oscillations in the two NSs with typical amplitudes $\delta\rho_{\max}/\rho_{\max} \sim 0.15$. More accurate initial data could be obtained using the methods described in East, Ramazanoğlu & Pretorius (2012b) or Moldenhauer et al. (2014). Alternatively, the errors in the constraint could be mitigated adopting constraint-damping formulations of the Einstein equations (Bernuzzi & Hilditch 2010; Alic et al. 2012; Weyhausen, Bernuzzi & Hilditch 2012; Alic, Kastaun & Rezzolla 2013; Hilditch et al. 2013; Kastaun et al. 2013). Note, however, that none of these methods, with the exception of Moldenhauer et al. (2014), solves for the hydrostatic equilibrium and can remove all of the oscillations. We leave the investigation of these methods to future work.

We construct the quasi-circular (low eccentricity) initial data using the `LORENE` pseudo-spectral elliptic solver (Gourgoulhon et al. 2001). We setup irrotational initial data at a separation of 45 km consisting of NSs each having gravitational mass at infinite separation $M_\infty = 1.384\,M_\odot$ and baryonic mass $M_b = 1.515\,M_\odot$.

For the evolution we make use of the adaptive mesh refinement (AMR) capabilities provided by the `Carpet` (Schnetter, Haley & Hawke 2004) mesh refinement driver for `Cactus` (Goodale et al. 2003). During the inspiral, we employ a grid composed of five refinement levels with the finest ones composed of boxes that move to follow the centres of the two NSs. After merger, we switch to a fixed grid, also composed of five refinement levels. In both cases, the finest grid, which covers the two neutron stars and the merger remnant, has a grid spacing of $h = 0.145\,M_\odot \simeq 215$ m. We also perform a simulation at lower resolution with $h = 0.25\,M_\odot \simeq 369$ m to estimate finite-resolution effects on our simulations. To reduce the computational cost, we exploit the symmetries of the problem to restrict our calculations to $x \geq 0$, $z \geq 0$: rotational symmetry is used across the yz −plane and reflection symmetry is uses across the xz −plane.

3 RESULTS

3.1 Overall dynamics

Eccentric and quasi-circular BNS mergers have rich dynamics that can lead to a number of outcomes depending on the EOS, masses, and orbital parameters of the binary (Shibata & Taniguchi 2006; Baiotti, Giacomazzo & Rezzolla 2008; Rezzolla et al. 2010; East & Pretorius 2012; Gold et al. 2012; East et al. 2016; Paschalidis et al. 2015). This is also reflected in the dynamics of our simulations. Binaries with small Newtonian periastron radii (`RP0` – head-on collision – and `RP5`) result in prompt BH formation and negligible amount of unbound mass. Binaries with larger Newtonian periastron radii, e.g. `RP7.5`, and quasi-circular binaries (`QC`) result in the formation of hypermassive neutron stars (HMNSs) (Baumgarte, Shapiro & Shibata 2000), meta-stable massive remnants temporarily supported against gravitational collapse by a large degree of differential rotation (Baiotti et al. 2008; Kaplan et al. 2014). Binaries with larger Newtonian periastron radii (models `RP10` and `RP15`) result in multiple close encounters. The `RP10` model, in particular, has a very complex dynamics and undergoes three close encounters, before finally merging after the third encounter. The `RP15` model is also expected to undergo multiple encounters, however the timescales between successive encounters is too long to be simulated with our methods, so we only consider its first close passage.

The orbital dynamics of the `RP10` model appears to be very sensitive to small changes in the simulation inputs and, in our preliminary tests, we observed differences in the timing and number of encounters with changes in the numerical parameters (e.g. resolution). A similar behaviour is also observed in eccentric binary BHs encounters (Damour et al. 2014, Guercilena, priv. comm.). For this reason, the `RP10` simulations should be considered as particular realizations of the dynamics close to the threshold between direct merger and multiple encounters and not necessarily as the outcomes of encounters with r_p exactly equal to 10 $M_\odot$. Indeed, the precise *value* of this threshold is probably the imprint of our numerical setup and is likely to change once this setup is varied. On the other hand, the *existence* of such a threshold will not depend on the numerical details. The orbital dynamics of the other binaries, instead, appears robust. The accuracy of numerical relativity simulations of quasi-circular BNS inspirals has been studied in detail in the past (Baiotti, Giacomazzo & Rezzolla 2009; Baiotti, Shibata & Yamamoto 2010; Bernuzzi, Thierfelder & Brügmann 2012, Radice et al. 2014a, 2014b, 2015).

The dynamics of binary `LK_RP10` is shown in Fig. 1. There we plot colour maps of the rest-mass density in the orbital plane at representative times during the evolution (before and after each close encounter). During the periastron passage strong tidal torques and shocks result in episodic outflow events. Part of the ejected neutron-rich matter is unbound from the system (more on this in Section 3.2), while the rest settles in a thick atmosphere around the NSs. The atmosphere is mostly thermally supported in the purely hydrodynamic `HY_RP10` simulation, but not in the simulations which include neutrino cooling. In the latter cases, the 'envelope' around the binary has time to cool and partly accrete back on to the NSs in the time between successive encounters. This results in the `LK_RP10` simulation undergoing its last encounter ∼2 ms before `HY_RP10`.

The encounters also excite oscillations of the two NSs, which result in copious GW emission. This phenomenon has been previously reported in simulations employing idealized EOS (Gold et al. 2012; East & Pretorius 2012) and studied in detail by Gold et al. (2012). They showed that tidal interactions during close encounters can excite the fundamental modes of oscillation of the two NSs. This is apparent in our `RP10` model whose curvature GW signal, the Weyl scalar Ψ_4,[1] is shown in Fig. 2. The first encounter is accompanied by a burst in GWs followed by a quasi-periodic signal lasting about ∼10 ms, i.e. up to the time of the second encounter. For all of the `RP10` simulations, we find the interaction between the two NSs during the second encounter to suppress the oscillations of the two stars leading to a sudden shutdown of the GW emission. This is an effect that has not been reported before. However, it may be a consequence of the π −symmetry imposed during the evolution. More simulations would be required to address this question. A second, sudden, burst in GWs appears at the time of merger.

Like the orbital dynamics of the binaries before the merger, also their post-merger evolution shows a large variety. As discussed

[1] We remind the reader that the complex scalar Ψ_4 combines the second time derivatives of the two strain polarizations $\Psi_4 = \ddot{h}_+ - \mathrm{i}\,\ddot{h}_\times$.

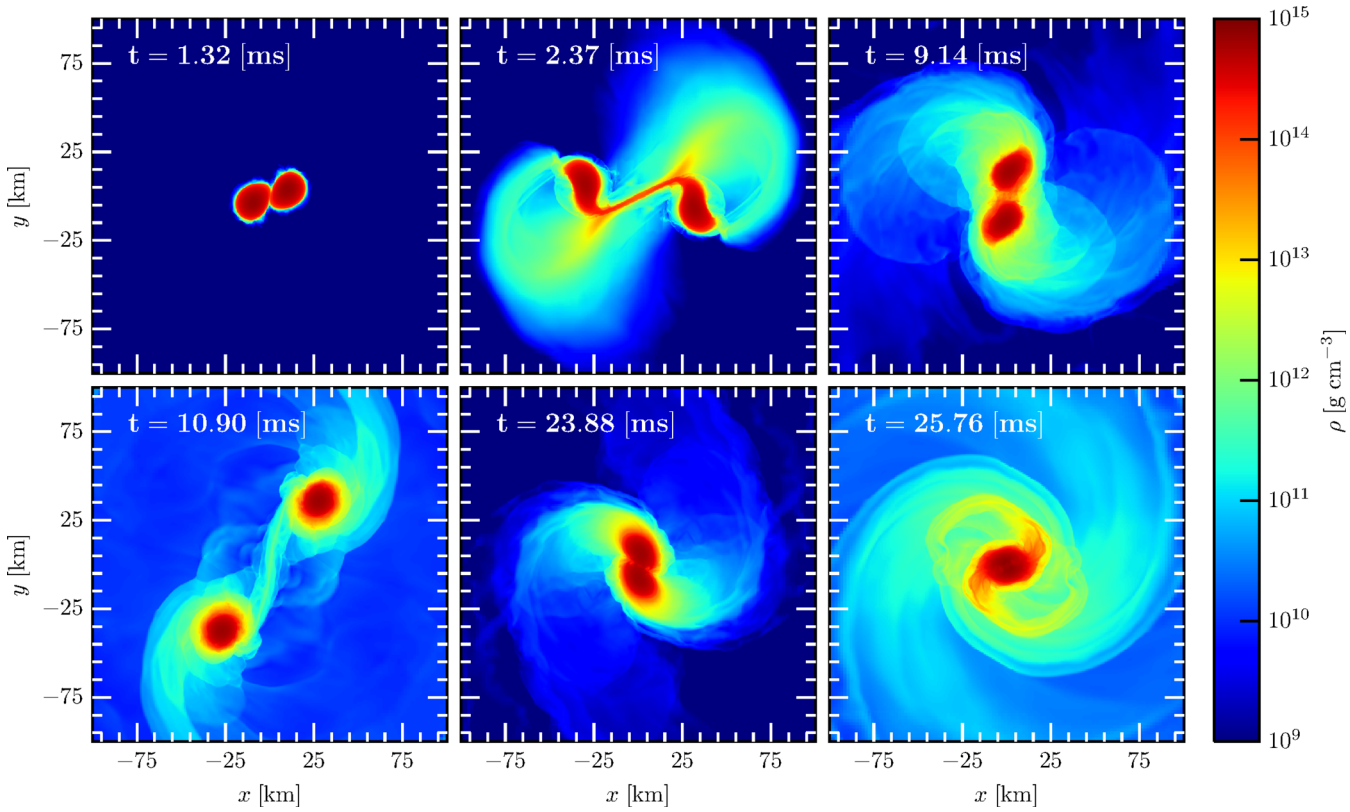

Figure 1. Rest-mass density (equation 4) in the orbital plane for the parabolic encounter simulation LK_RP10 at six different times. The NSs undergo three close encounters before merging. The panels show snapshots of the two stars immediately before and after each encounter. Tidal torques at the periastron result in large mass ejection and trigger oscillations in the NSs, cf. Fig. 2.

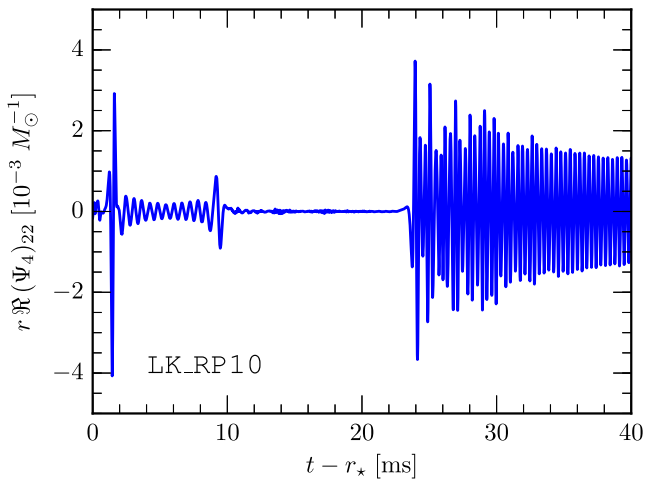

Figure 2. Real part of the $\ell = 2, m = 2$ spin-weighted spherical harmonics component of the Weyl scalar Ψ_4 for the LK_RP10, extracted at $r_\star = 400\,M_\odot \simeq 590$ km. The curvature GW signal shows a burst after the first encounter that excites violent oscillations in the two NSs. These oscillations are then suppressed by tidal interactions during the second encounter. The GW signal turns on again at merger.

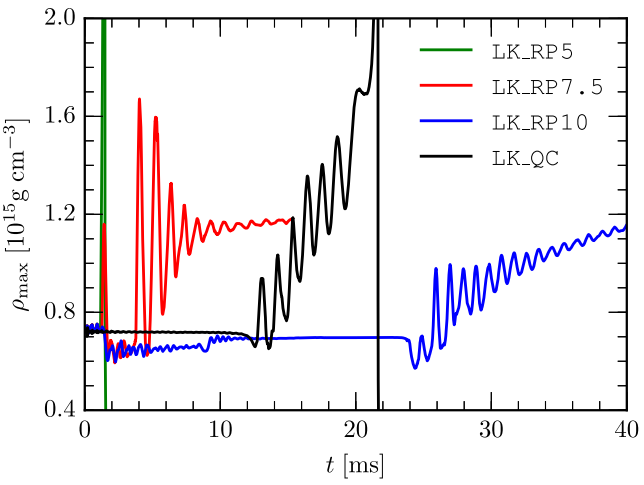

Figure 3. Maximum rest-mass density (equation 4) as a function of time for the simulations with neutrino cooling, LK runs. The LK_RP runs are with eccentric binaries, while the LK_QC is quasi-circular. Although all of the models have almost the same mass and we use a single EOS, there is significant variability in the outcome of the merger due to the differences in the amount of angular momentum of the binary at merger.

above, the merger can result in prompt BH formation for binaries with little angular momentum (RP0, RP5) or in the formation of an HMNS. Furthermore, since different models merge with different amount of residual angular momentum and mass, the structure and rotational configuration of the HMNS can vary significantly leading to different evolutionary paths.

This is summarized in Fig. 3, where we show the maximum rest-mass density as a function of time for a group of representative simulations. The RP5 model exhibits prompt collapse: the central density rapidly grows until an apparent horizon is formed. After the formation of the apparent horizon, $\rho_{\max}$ appears to drop, because we exclude the region inside the BH in the calculation of the maximum

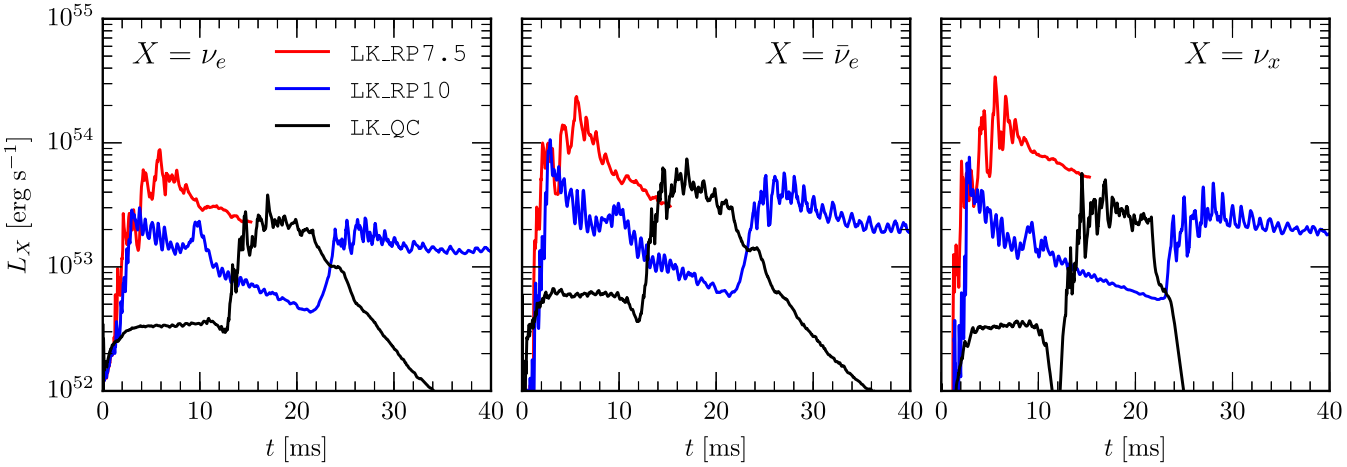

Figure 4. Neutrino luminosity for runs LK_RP7.5, LK_RP10, and LK_QC. Left-hand panel: electron neutrino luminosity. Middle panel: electron anti-neutrino luminosity. Right-hand panel: total luminosity from heavy lepton (μ, $\bar{\mu}$, τ, $\bar{\tau}$) neutrinos. Models with small periastron radius, such as LK_RP7.5, result in violent mergers with very bright neutrino bursts.

density. The RP7.5 model experiences a rather violent merger: the two stellar cores collide, slightly overshoot each other, and then merge again after ∼2 ms. In comparison, the quasi-circular model QC experiences a much milder merger, with a smaller initial jump in the density. However, since the QC binaries merge with smaller residual total angular momentum than the RP7.5 binaries, the resulting HMNS contracts and oscillates violently before collapsing to a BH within ∼10 ms after merger. Finally, the RP10 binary merges with a large amount of residual angular momentum, which sustains the hypermassive merger remnant over the entire simulated time ($\gtrsim$20 ms after merger).

We report the remnant torus masses for those binaries resulting in BH formation within the simulated time in Table 1. The torus masses are quoted at 1 ms after the formation of the apparent horizon. We find very small torus masses ($<10^{-2}\,M_\odot$) for the nearly head-on eccentric mergers, which result in prompt BH formation. Larger torus masses (∼few × $10^{-2}\,M_\odot$) are found for the QC models. The latter, however, vary by more than a factor of two depending on the level of microphysical description. The purely hydrodynamical simulation produces the largest torus mass and the simulation including neutrino cooling, but not heating, produces the smallest.

The diversity in the merger dynamics is also reflected in the neutrino signals shown in Fig. 4. The violent merger in the LK_RP7.5 simulation results in neutrino luminosities in excess of 10^{54} erg s^{-1} sustained over multiple milliseconds. These luminosities are comparable to those reported by Rosswog et al. (2013), who, however, performed simulations using Newtonian gravity and a different nuclear EOS. These luminosities are almost an order of magnitude larger than for our fiducial quasi-circular simulation (model QC_LK). The LK_RP10 simulation displays sudden rises in its neutrino emissions in coincidence with each close encounter, followed by cooling phases where the luminosity drops exponentially in time. Finally, the QC_LK run shows a single burst in its neutrino emission at the time of merger, followed by a rapid decay in its luminosity as soon as the HMNS collapses to a BH. The early time, $t \lesssim 12$ ms, neutrino emissions from the QC_LK simulation are due to the spurious heating of the surface of the two NSs caused by our numerical scheme. These early-time neutrino energy losses might appear large, but they are actually not dynamically important as they are ∼2 orders of magnitude smaller than the GW luminosity, which peaks at ∼2 × 10^{55} erg s^{-1} at the time of merger.

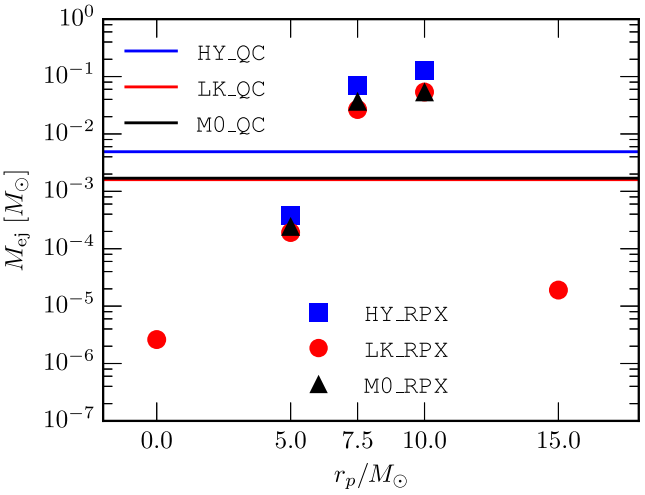

Figure 5. Dynamically ejected mass for all simulations as a function of the Newtonian periastron radius r_p. The ejecta mass is computed integrating in time the flux of unbound matter (with $u_t \leq -1$) across the surface of a spherical sphere with radius $r = 200\,M_\odot \simeq 295$ km. The horizontal lines denote the ejected mass from the quasi-circular runs. The ejecta for models with $r_p = 0$ and $r_p = 15\,M_\odot \simeq 22.15$ km are under-resolved and should not be taken at face value. Overall, eccentric binaries can eject up to 2 orders of magnitude more mass than quasi-circular binaries.

3.2 Dynamical ejecta

3.2.1 Ejected mass

Being on Newtonian parabolic orbits, our eccentric BNS binaries are only weakly bound. For this reason, it is not surprising to find that they can unbind a significantly larger amount of matter compared to quasi-circular mergers. Fig. 5 shows the total amount of unbound matter for each of our simulations (also reported in Table 1). The total ejected rest mass is computed integrating in time the flux of matter with $u_t \leq -1$[2] across a spherical coordinate surface with

[2] See Kastaun & Galeazzi (2015) for a discussion of possible alternative criteria to identify unbound fluid elements.

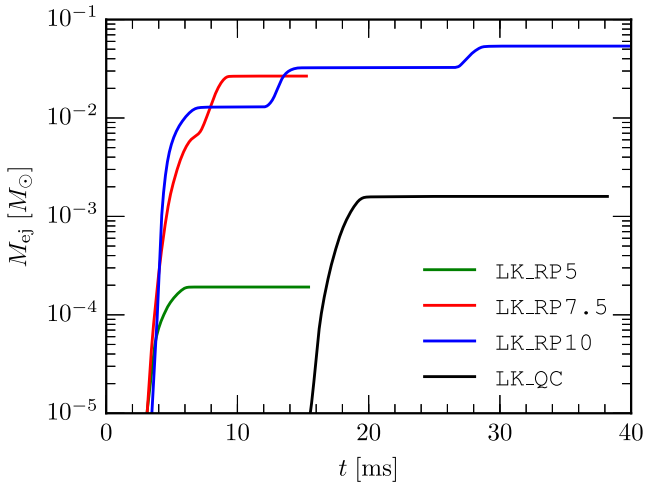

Figure 6. Total ejected mass for the LK_RP5, LK_RP7.5, LK_RP10, and LK_QC models. The ejecta mass is computed by integrating the flux of unbound matter (with $u_t \leq -1$) across a coordinate-sphere with radius $r = 200\,\mathrm{M}_\odot \simeq 295$ km. The dynamical mass ejection is impulsive and lasts only a few milliseconds.

radius $200\,\mathrm{M}_\odot \simeq 295$ km. We find that this choice can result in an underestimate of the total ejecta mass by up to ∼20 per cent as more material can become unbound at larger radii. However, the data extracted from larger radii is potentially affected by unphysical artefacts, because the density drops to values closer to the floor and the assumption of nuclear statistical equilibrium (assumed in our EOS treatment) is violated. Also note that these estimates do not include late-time mass ejection driven by neutrino, viscous heating, and/or magnetic pressure, which would take place on longer time-scales (Dessart et al. 2009; Fernández & Metzger 2013; Metzger & Fernández 2014; Siegel, Ciolfi & Rezzolla 2014; Ciolfi & Siegel 2015; Fernández et al. 2015a,b; Just et al. 2015; Kiuchi et al. 2015a; Martin et al. 2015; Rezzolla & Kumar 2015).

As shown in Fig. 6, the dynamical mass ejection in our simulations is impulsive and concentrated in one or, in the RP10 models, three ejection events lasting only several milliseconds. For this reason, our measure of the dynamically ejected mass is robust with respect to the physical time covered by our simulations.

Some interesting trends can be observed from Fig. 5. First of all, we find that eccentric mergers, and in particular mergers with impact parameters close to the threshold between prompt merger and multiple-encounters, seem to be those resulting in the largest mass ejection. This is similar to what was found by East & Pretorius (2012). Note that the RP15 model is likely to experience more mass ejection in its successive encounters, which will happen over time-scales that we cannot simulate directly. Nevertheless, we still expect encounters such as that of the LK_RP15 run to yield lower ejecta mass compared to encounters resulting in mergers over a short dynamical time-scale, such as RP7.5 and RP10. The reason for this is that model RP15 will undergo merger in a more gravitationally bound state than model RP7.5 or model RP10. As a consequence, we conjecture on the basis of our data that eccentric BNS mergers can yield up to $\sim 0.1\,\mathrm{M}_\odot$ of ejecta, slightly less than what can be achieved with BHNS mergers (Foucart et al. 2014; Kyutoku et al. 2015), but almost two orders of magnitude larger than what is ejected by mergers of BNSs in quasi-circular orbits.

We find significant differences between the LK results, which include neutrino cooling, and the HY, which neglect it. For all our models we find that neglecting neutrino cooling results in an overestimate of the unbound mass by a factor of $\gtrsim 2$. This hints at the importance of neutrino-radiation processes in shaping the outflows from these mergers. As documented in detail by Hotokezaka et al. (2013) and Bauswein et al. (2013), a significant fraction of the ejecta in GR simulations is driven by shocks. In our simulations neutrino losses in the optically thin outflows are rapid and sufficient to cause part of the material to become gravitationally bound again by removing part of its internal energy. In addition, the total amount of mass ejected by the RP10 binaries is also affected by the cooling of the thick atmosphere generated during the first encounter of the two NSs, which is suppressed in the HY_RP10 run, as discussed in Section 3.1.

The differences between models including only cooling (LK) and models also including heating (M0) are also important, but less striking. We find that the inclusion of heating results in a slight increase of the total ejected mass, similarly to what has been reported by Sekiguchi et al. (2015).

3.2.2 *Properties of the outflow*

We collect composition, specific entropy, asymptotic velocity and angular distribution of the ejecta for the three most interesting models, RP7.5 (representative of a violent collision), RP10 (representative of the dynamics with multiple encounters), and QC (our fiducial quasi-circular binary) in Fig. 7. The histograms are generated by binning the properties of the unbound matter (with $u_t \leq -1$) flowing through a coordinate sphere with radius $r = 200\,\mathrm{M}_\odot \simeq 295$ km. As can be seen from Fig. 7, morphology and thermodynamical properties of the ejecta show large variations with binary configuration and neutrino treatment. This is a consequence of the complex interplay, between radiation and hydrodynamics, that controls the mass ejection.

The electron fraction of the ejecta is one of the most important quantities determining both the outcome of the nucleosynthesis (more in Section 3.3) and the properties of the EM signature of the merger (see Section 3.4). It is also the quantity showing the greatest variation. Simulations neglecting all weak interactions are, unsurprisingly, characterized by extremely neutron-rich ejecta. In these simulations, Y_e is simply advected with the flow and unchanged. On the other hand, when weak interactions are included, Y_e can evolve due to electron or positron captures in shock-heated material (in the LK and M0 simulations) and due to neutrino absorption (in the M0 simulations). As a consequence, simulations accounting for weak interactions show a much wider range of electron fractions.

Independent of binary parameters, we find the ejecta to have a clear bi-modal distribution in Y_e. Part of the outflow, driven by tidal torques, is cold and neutron rich, while another component, launched by shocks during merger, experiences high-temperatures and rapid protonization with values of Y_e peaking at ∼0.16. The M0 simulations also show a relatively proton-rich $Y_e \simeq 0.4$ component of the outflow, predominantly at high latitudes (more on this later). The final mass distribution of Y_e depends on the relative importance of these different components.

The composition of the ejecta from our simulations is somewhat more neutron rich than that of Wanajo et al. (2014) and Sekiguchi et al. (2015). These studies appear to be lacking any cold component in their outflows. This might be a consequence of the different treatment of the neutrino radiation or of the choice of EOS. Instead,

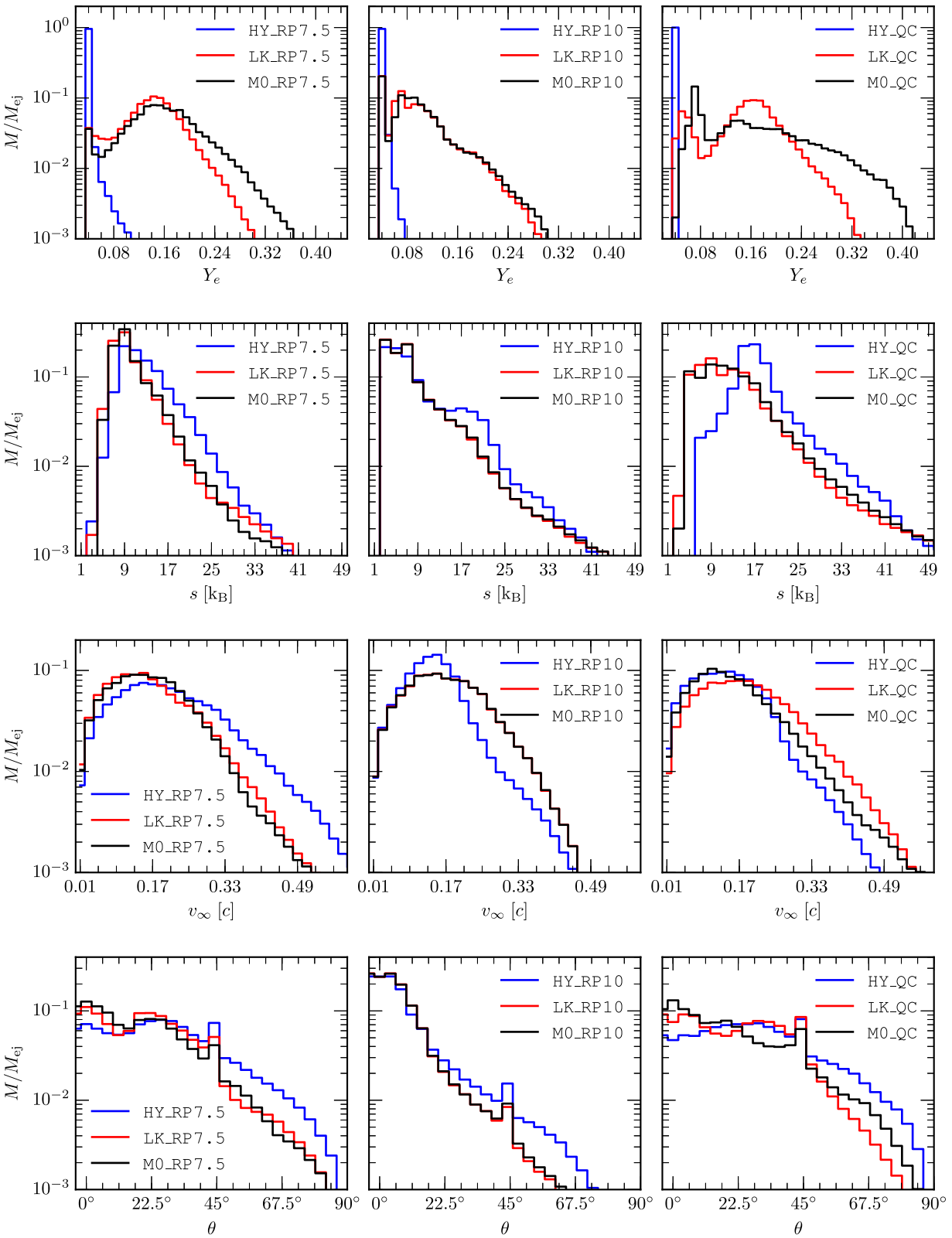

Figure 7. Electron fraction (top row), specific entropy per baryon (second row), asymptotic velocity (*third row*), and angular distribution (bottom row) of the ejecta. θ is the angle from the orbital plane. The first, second, and third columns show results from models `RP7.5`, `RP10`, and `QC` respectively. For each configuration we consider three different levels of microphysical description: pure hydrodynamics (`HY`), neutrino cooling (`LK`), or neutrino cooling and heating (`M0`). The histograms are computed from the mass fraction of the matter crossing a spherical surface at radius $r = 200\,M_\odot \simeq 295$ km with positive specific energy (i.e. with $u_t \leq -1$). The bump in the angular distribution at $\theta = 45^\circ$ is a numerical artefact generated by our Cartesian simulation grid.

we find good qualitative agreement between our LK_QC results and those of Palenzuela et al. (2015), who adopted different EOS, but a neutrino cooling treatment very similar to ours. Our ejecta are also significantly more proton-rich than those typically found in Newtonian simulations (e.g. Rosswog et al. 2013), where the tidal component is enhanced with respect to GR simulations (Bauswein et al. 2013).

The composition of the ejecta differs between eccentric and quasi-circular mergers. The reason for this is that eccentric mergers producing large ejecta mass do so mostly as a consequence of the enhanced tidal interaction between the two NSs during close passages. As a consequence, only nearly head-on collisions (model RP5) result in more proton-rich ejecta than the QC binaries (see Table 1). This trend is the *opposite* of what has been reported in Newtonian simulations, where quasi-circular binaries are dominated by tidal ejecta with low-Y_e and eccentric binaries by shock-heated, high-Y_e, ejecta (Rosswog et al. 2013). The LK_RP7.5 simulation has ejecta composition that is very similar to that of the quasi-circular LK_QC, while the multiple encounter simulation LK_RP10 has significantly more neutron rich ejecta than both.

The effect of neutrino absorption on the electron fraction is non-negligible, as also found by Wanajo et al. (2014), Sekiguchi et al. (2015), and Foucart et al. (2016), although in our simulations the impact is less significant than in these previous studies. The M0 runs have more proton rich ejecta than the LK simulations, but the differences appear to be mostly confined to the tail of the ejecta distribution in Y_e, while the mass-weighted average of the electron fraction $\langle Y_e \rangle$ is not strongly affected (cf. Table 1 and Fig. 7).

As can be seen from the second row of Fig. 7, the specific entropy per baryon of the ejecta shows somewhat smaller differences between simulations than Y_e. The overall trend is that runs that include neutrino cooling effects (LK and M0) display lower specific entropies than purely hydrodynamical models, which overestimate the final entropy of the shock-heated ejecta.

We find the bulk of the outflow to be sub-relativistic with asymptotic velocities $v_\infty \lesssim c/3$ (third row of Fig. 7) for both eccentric and quasi-circular models. This is in contrast with Newtonian simulations (Rosswog et al. 2013), but is similar to other GR studies (East & Pretorius 2012; Sekiguchi et al. 2015; East et al. 2016). There are some differences in the asymptotic velocities between HY, LK, and M0 simulations, but there is no clear trend.

We show the angular distribution of the ejecta in the bottom row of panels in Fig. 7. We find the outflow of the RP10 model, which ejects matter mostly due to tidal torques during its multiple encounters, to be mostly contained in a narrow angle around the orbital plane. This is similar what found for the ejecta of BHNS mergers (Foucart et al. 2014; Kyutoku et al. 2015). The other models show a larger angular spread of the outflow with the bulk of the ejecta appearing to be contained within an angle $\theta \lesssim 60^\circ$ of the orbital plane. The bump in the ejecta distribution function at $\theta = 45^\circ$ is a numerical artefact associated with our Cartesian simulation grid that tends to funnel flows along its symmetry directions.

The amount of ejected material at high latitudes ($\theta \gtrsim 60^\circ$) is also strongly dependent on the included physics in our simulations. Runs that do not include neutrino cooling tend to overestimate, by a factor of a few, the amount of matter in the polar region of the post-merger remnant. Conversely, simulations that include neutrino cooling, but not heating, underestimate the baryon contamination of the poles by a similar factor. These differences might have an impact for the simulation of SGRB engines, because baryon contamination of the polar regions might prevent the launch of relativistic jets in some SGRB models (e.g. Just et al. 2016).

3.2.3 *Ejection mechanisms*

In Fig. 8, we show the angular density and Y_e distribution of the ejecta for two of the quasi-circular BNS simulations: LK_QC and M0_QC. These profiles hint at the interplay between a few distinct mechanism for the dynamical ejection of NS matter. A first component of the outflow is driven by tidal interactions between the NSs. It is very neutron rich, with $Y_e \lesssim 0.1$, and confined in a narrow $\sim 20^\circ$ angle from the orbital plane. In our simulations, this is the first component to reach the fiducial outflow surface at $t \simeq 16$ ms (i.e. $\simeq 3$ ms after the merger; consistent with an outflow velocity of $\sim c/3$). This component is present in all of our simulations, regardless of their level of microphysical description.

A second component is driven by shocks launched during merger. It is less neutron rich, with $Y_e \sim 0.15$, and more isotropic, spanning an angular region of about 60° from the orbital plane. Shock driven ejecta lag the tidal tails by a few ms.

Finally, a third component is constituted by a high-latitude wind driven by a combination of shock and neutrino heating. This component is relatively proton rich with $Y_e \gtrsim 0.25$. It is mostly absent in the LK_QC simulation, but becomes the dominant outflow component after $t \simeq 21$ ms in the M0_QC run. The thermal wind also entrains a small part of the accretion torus resulting in additional low-Y_e material being ejected close to the equatorial plane at late times.

The interplay between low-Y_e (close to the equator) and high-Y_e (at high latitudes) ejecta is what determines the final electron fraction distribution of the ejecta (Fig. 7) and the r-process yields (more in Section 3.3).

3.3 Nucleosynthesis

As the material ejected during merger expands, it undergoes neutron capture nucleosynthesis, which may produce r-process elements. In order to estimate the final nucleosynthetic yields of our simulations, we map our ejecta data on to the grid of parametrized r-process calculations presented in Lippuner & Roberts (2015). First, we extract Y_e, s, v, and ρ for all of the unbound matter (with $u_t \leq -1$) as it flows across the surface of a coordinate sphere of radius $r_E = 200\,\mathrm{M}_\odot \simeq 295$ km. To estimate the nucleosynthesis in the outflow using our nucleosynthesis grid, the dynamical time-scale, τ, of each ejected fluid element is required. To estimate τ, we assume that the material crossing our extraction surface is expanding homologously. This assumption should be relatively well satisfied by our data given that, by the time the ejecta reach the detection surface, their density has already dropped by ~ 3 orders of magnitude. Then, the density history for a particular element of the ejecta is given by $\rho(t) = \rho_E (v_E t / r_E)^{-3}$, where ρ_E and v_E are the density and velocity of the fluid element when it crosses a sphere of radius r_E. At late times, the density history used in Lippuner & Roberts (2015) has the form $\rho(t) = \rho(s,\, Y_e,\, T = 6\,\mathrm{GK})(3\tau/et)^3$, where e is Euler's number. We match these two profiles to extract τ. The final yields are then found by multiplying the yields computed by Lippuner & Roberts (2015) at each point in their nucleosynthesis grid with the total mass associated with it. Such a procedure is necessarily approximate, but it enables the rapid calculation of the abundance distribution in the ejecta without the need for tracer particles. Future work should directly compare this method of yield estimation to more detailed tracer-particle based methods.

We do not find material with expansion time-scale of less than 0.5 ms. This seems to exclude the neutron freeze-out scenario proposed by Metzger et al. (2015). However, the lack of a very fast

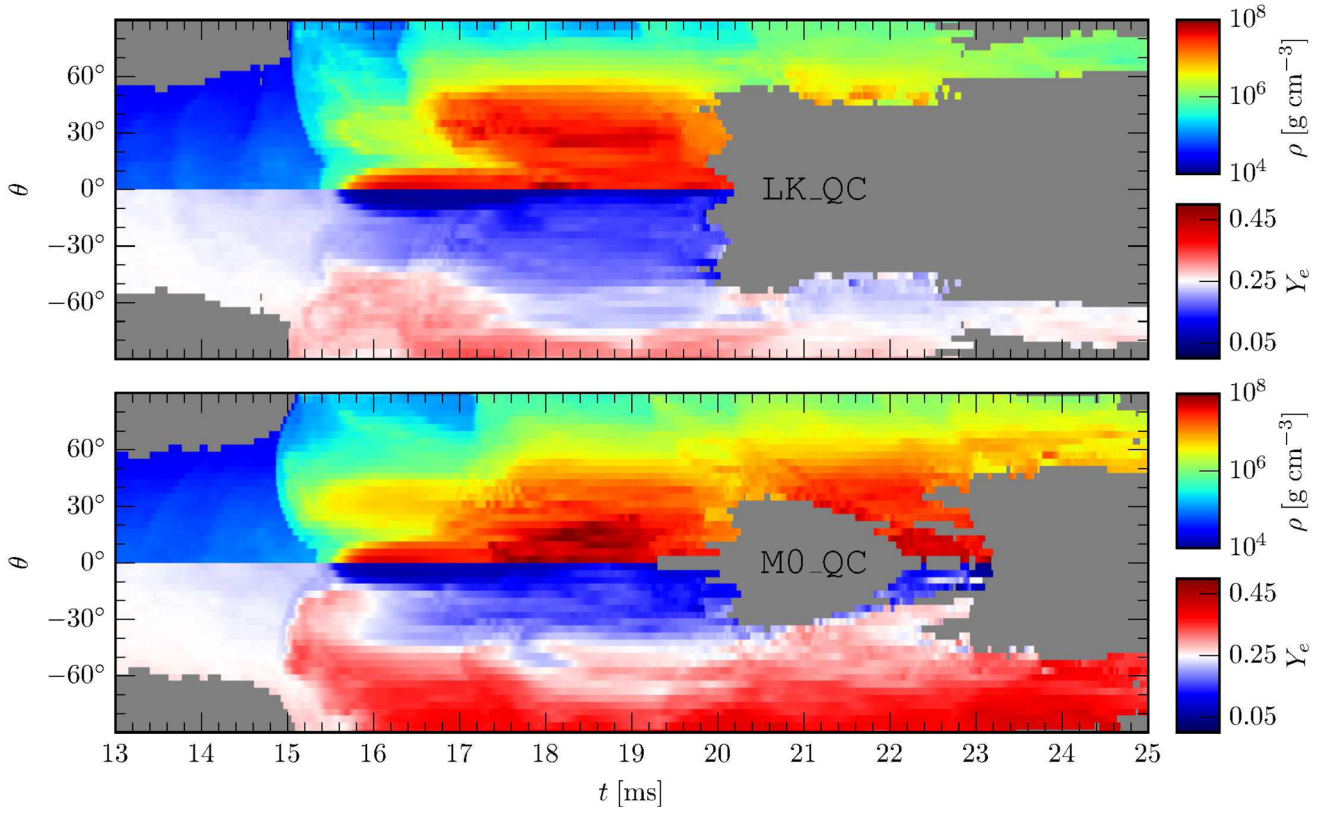

Figure 8. Angular distribution (upper half of each panel) and composition (lower half of each panel) of the ejecta for the LK_QC (upper panel) and M0_QC (lower panel) simulations as a function of time. The data is collected on a coordinate sphere at radius $r = 200\,M_\odot \simeq 295$ km and only considers the unbound part of the outflow (i.e. with $u_t \leq -1$). The grey shaded areas refer to times/angles for which we do not measure any outflow of unbound matter (i.e. where $u_t > -1$). The ejection event is of very short duration and the outflow is confined within a broad $\sim 60^\circ$ angle from the equator. The material at low altitudes is typically more neutron rich than at higher altitudes, suggesting a different ejection mechanisms for the different components of the outflow.

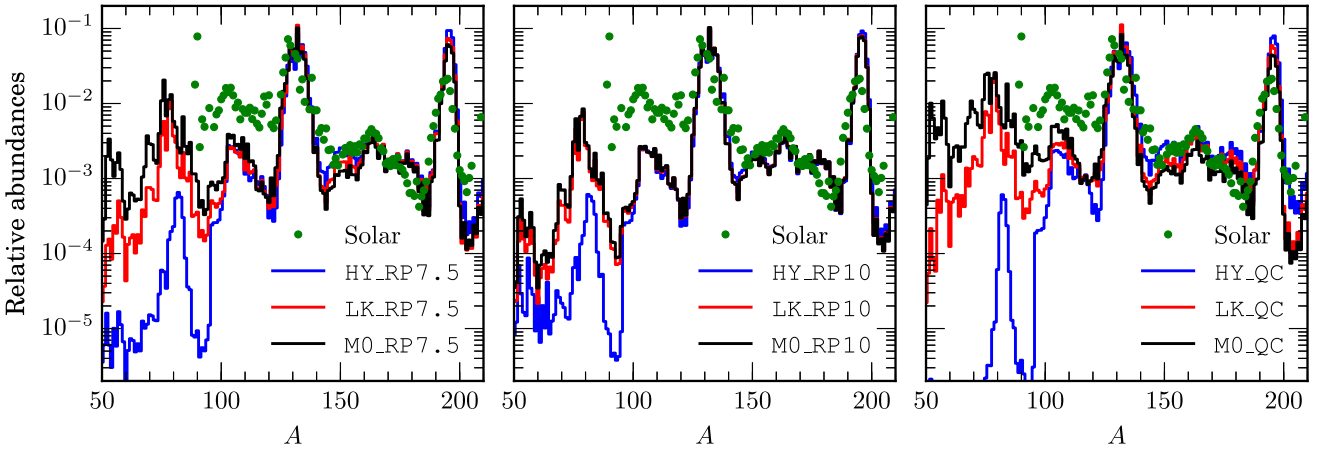

Figure 9. Final abundances in the ejecta for the RP7.5, RP10 and QC configurations. The yields are normalized with the total abundance of elements with $63 \leq A \leq 209$. For each configuration we consider three different levels of microphysical description (pure hydrodynamics, HY or leakage with only cooling, LK, or with heating/absorption included, M0). The abundance pattern for elements with $A \gtrsim 120$ is very robust and in overall good agreement with the Solar r-process abundances taken from Arlandini et al. (1999).

component of the ejecta might also be due to numerical effects. Our resolution is probably not high enough to track the very small fraction of the ejecta expected to experience neutron freeze-out in the scenario proposed by Metzger et al. (2015).

We show the results of this procedure in Fig. 9, where we plot the relative abundances of different elements in the final composition of the ejecta for three of our models (RP7.5, RP10, and QC) and with three different levels of microphysical description (HY, LK, and M0). The dynamical ejecta from all our simulations is neutron rich with mass-averaged electron fractions $\langle Y_e \rangle \lesssim 0.2$ (see Fig. 7). We show the joint distribution of Y_e and specific entropy per baryon s for simulation QC_M0 in Fig. 10. There is an approximate correlation between Y_e and s, due to the fact that shock heated material undergoes more weak processing. However, the critical

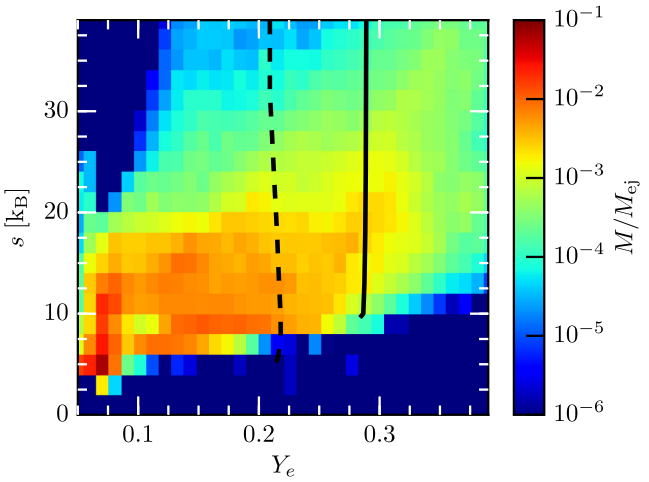

Figure 10. Joint distribution of composition and entropy for the `M0_QC` simulation. The material to the left of the dashed contour line produces second and third r-process nucleosynthesis, while material to the right of the solid contour line only produces first peak r-process nucleosynthesis. The figure also hints at the existence of a correlation between Y_e and s as larger proton fractions are typically found in combination with high entropies.

electron fraction for producing third-peak r-process elements is relatively insensitive to s (see the contour lines in Fig. 10). The bulk of the ejecta lies in a region of parameter space where a robust r-process will occur. In fact, we find that fission cycling occurs in most of the material. As a result, we find the relative abundances for $A \gtrsim 120$ to be robust and close to Solar, regardless of the merger type (eccentric versus quasi-circular) and of the neutrino treatment. The only minor difference we find is that eccentric mergers show a slight increase in the production of third-peak region nuclei, due to their more neutron-rich ejecta.

The yields for $50 \lesssim A \lesssim 90$, referred to here as the first-peak region, show greater variability than the yields at larger A. Material in this atomic mass range is produced in ejecta with $Y_e \gtrsim 0.22$, where an incomplete r-process occurs. Material quickly builds up in the first and second peaks and then gets left there due to early neutron exhaustion. The amount of material with $Y_e \gtrsim 0.22$ is sensitive to both the binary parameters and the treatment of neutrinos. Without weak interactions, in the `HY` models, almost all of the ejected material undergoes a complete r-process for all of the binaries. In the models including electron and positron captures but not neutrino captures (`LK`), there is less first peak region material for the eccentric BNS mergers, which have slightly more neutron rich ejecta than the quasi-circular mergers. The further inclusion of neutrino captures in the `M0` models has the largest impact on the yields of the `QC` model. This is likely due to its low average ejecta velocity compared with the eccentric mergers. None the less, neutrino captures only have a moderate impact on the final yields for all simulated binaries.

Because of the small amount of mass in the high Y_e tail of our ejecta, first-peak nuclei are underproduced with respect to the Solar abundances (when normalizing to the second r-process peak). Therefore, we cannot account for all of the r-process yields in the dynamical ejecta of BNS mergers. This is in contrast with the results of Wanajo et al. (2014), who found first-peak region nuclei to be produced in approximately Solar proportion. Their simulations yield a much wider distribution of Y_e than ours and a larger fraction of their ejecta undergoes an incomplete r-process. The reasons for this discrepancy are unclear, but they could be due to differences in the EOS or in the treatment of neutrinos.

3.4 Electromagnetic counterparts

The energy released by the radioactive decay of r-process nuclei powers transients in the optical or near-infrared band that could potentially be discovered through GW or SGRB detection follow-up observations and by untargeted transient surveys.

We use a simple analytical model developed by Grossman et al. (2014) to describe the basic features of the macronova emission that would be produced by the ejecta from our simulations. Grossman et al. (2014) estimate the time at which the optical or near-infrared signal peaks as the time when the radiation diffusion time-scale is equal to the dynamical time-scale of the ejecta

$$t_{\rm peak} = 4.9 \left(\frac{M_{\rm ej}}{10^{-2}\,{\rm M}_\odot}\right)^{1/2} \times \left(\frac{\kappa}{10\,{\rm cm^2\,g^{-1}}}\right)^{1/2} \left(\frac{\langle v_\infty\rangle}{0.1\,c}\right)^{-1/2} {\rm d}\,, \quad (9)$$

where $M_{\rm ej}$ is the ejected mass, κ is an effective opacity of the ejecta, and $\langle v_\infty\rangle$ is the mass-averaged asymptotic velocity of the outflow. They also estimate the peak bolometric luminosity assuming a simple power-law decay for the energy release by the radioactive decay of r-process elements $\dot\epsilon = \dot\epsilon_0 (t/t_0)^{-\alpha}$:

$$L = 2.5\times10^{40} \left(\frac{M_{\rm ej}}{10^{-2}\,{\rm M}_\odot}\right)^{1-\alpha/2} \times \left(\frac{\kappa}{10\,{\rm cm^2\,g^{-1}}}\right)^{-\alpha/2} \left(\frac{\langle v_\infty\rangle}{0.1\,c}\right)^{\alpha/2} {\rm erg\,s^{-1}}\,. \quad (10)$$

Finally, the effective temperature can be computed assuming the area of the emitting surface to be $4\pi(\langle v_\infty\rangle t_{\rm peak})^2$, which yields (Grossman et al. 2014)

$$T = 2200 \left(\frac{M_{\rm ej}}{10^{-2}\,{\rm M}_\odot}\right)^{-\alpha/8} \times \left(\frac{\kappa}{10\,{\rm cm^2\,g^{-1}}}\right)^{-(\alpha+2)/8} \left(\frac{\langle v_\infty\rangle}{0.1\,c}\right)^{(\alpha-2)/2} {\rm K}\,. \quad (11)$$

The limitations of this simple model are discussed in Grossman et al. (2014) and the most serious one is that it tends to overestimate both peak time and luminosity compared to more sophisticated numerical treatments.

We report the estimated peak times, luminosities and effective temperatures for the macronova emission from our simulations in Table 1. The values we quote are obtained using $\kappa = 10\,{\rm cm^2\,g^{-1}}$ as the fiducial opacity of the r-process material. This value gives results that are consistent with those of more sophisticated Monte Carlo calculations with large data bases of lines (Barnes & Kasen 2013). For the energy production from the radioactive decay of the r-process elements we follow Grossman et al. (2014) and choose $\alpha = 1.3$.

As can be inferred from Table 1, the macronova time-scales and luminosities show significant variation between our simulations. Simulations such as `LK_RP5`, which result in very little ejecta, have macronovae that peak on very short time-scales (less than a day) and that are relatively blue compared to those of quasi-circular binaries. The `RP7.5` and `RP10` models, which eject significantly more material than the `QC` model, have macronova light curves that peak on a time-scale of one to two weeks. They are also characterized by

lower effective temperatures and higher intrinsic luminosities with respect to quasi-circular binaries. We also find the basic macronova properties to be rather sensitive to the level of microphysical description. For instance, the peak time for the quasi-circular binary goes from 2.8 d to 1.4 d or 1.6 d when including neutrino cooling or neutrino cooling and heating.

The ejecta are also expected to lead to radio emission as they transfer their kinetic energy to the surrounding interstellar medium and produce non-thermal synchrotron emission (Nakar & Piran 2011). The time-scale over which the ejecta are decelerated is given by (Nakar & Piran 2011)

$$t_{\rm dec} = 30 \left(\frac{E_{\rm kin}}{10^{49}\,{\rm erg}}\right)^{1/3} \times \left(\frac{n_0}{{\rm cm}^{-3}}\right)^{-1/3} \left(\frac{\langle v_\infty\rangle}{c}\right)^{-5/3} {\rm d}\,, \quad (12)$$

where n_0 is the density of the interstellar medium. Note that equation (12) may be overestimating the deceleration time, because it does not account for asphericities and non-uniform velocities in the outflows (Piran, Nakar & Rosswog 2013; Margalit & Piran 2015). However, our goal is not to provide detailed estimates of the radio light curve. These are difficult to construct in the light of the large uncertainties in the ejecta properties. Rather, we want to look for systematic trends. The simplified treatment we adopt should be sufficient for this purpose.

Plasma instabilities develop at the location of the moving blast wave, generating magnetic field and accelerating the electrons into a power-law spectrum $N(E) \propto E^{-p}$ with exponent p. At an observing frequency $\nu_{\rm obs}$ higher than both the self-absorption and synchrotron peak frequencies the radio fluence (i.e. the flux density per unit frequency) for a source at a distance D can be expressed as (Nakar & Piran 2011)

$$F_\nu = 0.3 \left(\frac{E_{\rm kin}}{10^{49}\,{\rm erg}}\right) \left(\frac{n_0}{{\rm cm}^{-3}}\right)^{\frac{p+1}{4}} \left(\frac{\epsilon_B}{0.1}\right)^{\frac{p+1}{4}} \times \left(\frac{\epsilon_e}{0.1}\right)^{p-1} \left(\frac{\langle v_\infty\rangle}{c}\right)^{\frac{5p-7}{2}} \left(\frac{D}{10^{27}{\rm cm}}\right)^{-2} \times \left(\frac{\nu_{\rm obs}}{1.4\,{\rm GHz}}\right)^{-\frac{p-1}{2}} {\rm mJy}\,, \quad (13)$$

where $\epsilon_{\rm B}$ and $\epsilon_{\rm e}$ are the efficiencies with which the energy of the blast wave is transferred to the magnetic field and to the electrons, respectively.

The properties of the radio remnant produced by the ejecta from our simulations are reported in Table 1. To compute $t_{\rm dec}$ and F_ν, we adopt $n_0 = 0.1\,{\rm cm}^{-3}$ as fiducial value for the number-density of the interstellar medium, which is a reasonable value for a GC (Rosswog et al. 2013). We also take $p = 2.3$, $\nu_{\rm obs} = 1.4$ GHz, and $\epsilon_{\rm B} = \epsilon_{\rm e} = 0.1$ following Nakar & Piran (2011). Finally, we place our binaries at a reference distance of $D = 3.086 \times 10^{26}$ cm $\simeq 100$ Mpc.

As with the macronova emission, we find significant variation in the properties of the radio transients emergent from our simulations. This is not surprising given that the deceleration time-scale and the radio fluence depend on the mean velocity and on the kinetic energy of the ejecta, which in turn change with model and neutrino treatment. The time-scale for the radio emission varies from $\sim$1 year to almost 30 yr between different simulations. The radio fluence varies by more than two orders of magnitude between all our runs, going from 0.015 mJy in simulation `M0_QC` to 2.170 mJy in simulation `HY_RP7.5`. Deceleration time-scale and fluence are also strongly dependent on the microphysical treatment. For instance, F_ν changes by almost a factor of 10 (from 2.170 mJy to 0.274 mJy) for the `RP7.5` model when switching on neutrino cooling.

4 SUMMARY AND DISCUSSION

In this study, we presented a number of full-GR numerical simulations of BNS mergers employing a microphysical EOS. We considered both mergers of binaries in quasi-circular orbits and of eccentric binaries produced through dynamical capture in dense stellar environments. We systematically varied the level of our treatment of weak reactions in our simulations to isolate the impact of neutrino emission and absorption on the composition and morphology of the outflows.

We identify three main components of the dynamical ejecta in our simulations. A first component, driven by tidal interactions between the two NSs, is cold and very neutron rich (with $Y_e \lesssim 0.1$), and it is confined within $\sim$20° of the orbital plane. A second component is driven by shocks formed during the merger and is less neutron rich with $Y_e \gtrsim 0.15$, but more isotropic, being spread over an angle of $\sim$60° from the orbital plane. A third, relatively proton-rich, with $Y_e \gtrsim 0.25$, but very tenuous, component is observed at high-latitudes, especially in simulations that include neutrino heating. The relative importance of each of these components varies between the simulations and is the result of the interplay between the bulk dynamics and the effects of neutrino transport. All of the ejecta are sub-relativistic with $\langle v_\infty\rangle \lesssim c/3$ for all but the most extreme, nearly head-on, configurations, which, however, result in very little ejecta, because of prompt BH formation.

In agreement with previous work (East & Pretorius 2012; Rosswog et al. 2013), we find that eccentric binaries can eject orders of magnitude more mass than binaries in quasi-circular orbits and only slightly less than BHNS binaries. Somewhat surprisingly, and different from Newtonian results (Rosswog et al. 2013), we find that the ejecta from eccentric mergers are typically more neutron rich than those of quasi-circular mergers. The reason for this is that the ejecta in eccentric mergers is increasingly dominated by the tidal component. This trend is the opposite of what is found in Newtonian simulations by Rosswog et al. (2013), which found eccentric mergers to yield more proton-rich outflows than quasi-circular mergers. The reason for this difference is that, on the one hand, Newtonian calculations tend to overestimate the relative ratio of tidally- to shock-driven ejecta for quasi-circular binaries (Bauswein et al. 2013). On the other hand, Newtonian studies also overestimate the amount of shocked ejecta for eccentric binaries.

Our results also indicate that neutrino cooling and heating have an important impact on the composition, morphology, total mass of the outflows, and remnant torus masses. Simulations performed neglecting neutrino cooling and heating consistently overestimate ejecta masses by a factor of $\sim$2 or more. They also over-predict the amount of mass ejected at high-latitudes by a factor of a few. Given the impact that baryonic pollution in the polar regions of SGRB engines may have (Just et al. 2016), this suggests that SGRB engine studies should use initial data from mergers simulations that included both cooling and heating from neutrinos.

The effect of neutrino heating on the total unbound mass is comparably smaller. However, we find the differences between simulations including or neglecting neutrino heating to be significant enough to suggest that neutrino heating should also be accounted for.

The absorption of neutrinos in the ejecta can also contribute to the protonization of the outflow. We find this effect to be appreciable in

our simulations, although not as significant as reported by Sekiguchi et al. (2015) and Foucart et al. (2016). The absorption of neutrinos seems to be affecting the mass-distribution of the ejecta at high-Y_e, and it is especially significant at high latitudes. At the same time, we find the variation in the average electron fraction of the ejecta to be small and, in some cases, insignificant. The differences between our results and those of Sekiguchi et al. (2015) and Foucart et al. (2016) could be due to the different treatments of neutrino radiation and hydrodynamics, or of the methodology employed in the analysis. We note that we find significant discrepancies in the composition of the ejecta with Sekiguchi et al. (2015), even when comparing simulations that did not include heating. Instead, we find good agreement with Palenzuela et al. (2015), who, however, used a different nuclear EOS.

We also find neutrino physics to have a significant impact on the basic characteristics of the EM counterparts from BNS mergers. Switching on neutrino cooling and heating can result in differences in the macronova peak times of several tens of percent and up to factors of a few in some cases. Even more drastic is the impact of the neutrino treatment on the properties of the radio remnants created by the mergers. For instance, the radio fluence at 1.4 GHz for one of our models changes by almost a factor of 10 when neutrino cooling is switched on. This is a consequence of the fact that the properties of the radio emission depend crucially on the asymptotic kinetic energy of the ejecta, which, is affected by the cooling.

We estimate the nucleosynthetic yields of our simulations using the tabulated yields of Lippuner & Roberts (2015). We find that, despite their very diverse nature, all considered BNS mergers (eccentric or quasi-circular) robustly produce r-process elements with atomic mass number $A \gtrsim 120$, with relative abundances close to the Solar r-process abundance distribution. At the same time, our yields show a deficit at lower A compared to the Solar abundances. This is different from what was reported by Wanajo et al. (2014). If confirmed, our results would suggest that either core-collapse supernovae or late-time neutrino, magnetically, and/or viscously driven winds (Dessart et al. 2009; Fernández & Metzger 2013; Metzger & Fernández 2014; Siegel et al. 2014; Ciolfi & Siegel 2015; Fernández et al. 2015a,b; Just et al. 2015; Kiuchi et al. 2015a; Martin et al. 2015; Rezzolla & Kumar 2015) would still be needed to produce the least massive of the r-process nuclei.

We find the neutrino-driven ejecta at high latitudes, within $\sim 30^\circ$ of the polar axis, to be relatively proton rich ($Y_e \gtrsim 0.3$) and mostly free of lanthanides. This material will become optically thin on short time-scales (i.e.less than a day, Kasen et al. 2013; Tanaka & Hotokezaka 2013). This may have consequences for the observation of macronovae counterparts to SGRBs, which are commonly believed to be associated with mergers seen face-on. In the case of a long-lived HMNS, the ejecta from the disc surrounding the HMNS may be sufficiently proton rich to be also Lanthanide free (Kasen, Fernández & Metzger 2015), so that the macronova will be dominated by the disc ejecta at early times, when the dynamical ejecta close to the equatorial plane are still optically thick. In this scenario, it may be possible to constrain the survival time of the HMNS, as suggested by Kasen et al. (2015). A possible uncertainty, however, is related to the interaction between the disc and the dynamical ejecta close to the equator, which may result in the disc wind ejecta being covered by the more optically thick dynamical ejecta. This will need to be addressed by future studies.

Important limitations of the present study are that we restricted ourselves to a single EOS and to equal mass binaries. We also ignored the effects of NS spin and of magnetic fields. Mass ejection may change quantitatively and possibly qualitatively with different EOS and with unequal mass binaries (Rezzolla et al. 2010; Bauswein et al. 2013; Hotokezaka et al. 2013; Dietrich et al. 2015; Palenzuela et al. 2015; Sekiguchi et al. 2015; Foucart et al. 2016), or with the inclusion of spin (Kastaun & Galeazzi 2015; East et al. 2016). While the pre-merger magnetic fields are probably too weak to impact the dynamical ejecta in quasi-circular binaries, this might change for eccentric binaries undergoing multiple encounters. This is so because magnetic fields might be significantly amplified by magnetohydrodynamical instabilities triggered when the two NSs come into contact at their periastron (Obergaulinger, Aloy & Müller 2010; Zrake & MacFadyen 2013; Kiuchi et al. 2015b). In this way magnetic fields could become dynamically relevant even before merger. Finally, given the qualitative and quantitative impact that neutrino radiation has on the ejecta, it will be necessary to validate or replace currently employed neutrino treatments with full multi-group (spectral) GR neutrino-radiation-hydrodynamics simulations. Addressing these issues will be object of future work.

ACKNOWLEDGEMENTS

We thank S. Bernuzzi, S. Richers, and S. Rosswog for useful discussions, and the anonymous referee for comments that have improved the paper. This research was partially supported by the Sherman Fairchild Foundation, by NSF under award nos. CAREER PHY-1151197, PHY-1404569, and AST-1333520, and by 'NewCompStar', COST Action MP1304. FG is supported by the Helmholtz International Center for FAIR within the framework of the LOEWE programme launched by the State of Hesse. Support for LFR during this work was provided by NASA through an Einstein Postdoctoral Fellowship grant numbered PF3-140114 awarded by the *Chandra* X-ray Center, which is operated by the Smithsonian Astrophysical Observatory for NASA under contract NAS8-03060. The simulations were performed on the Caltech compute cluster Zwicky (NSF MRI-R2 award no. PHY-0960291), on SuperMUC at the LRZ in Garching, on the NSF XSEDE network under allocation TG-PHY100033, on LOEWE in Frankfurt, and on NSF/NCSA BlueWaters under NSF PRAC award no. ACI-1440083.

REFERENCES

Abbott B. P. et al., 2016, Phys. Rev. Lett., 116, 061102
Acernese F. et al., 2015, Class. Quantum Gravity, 32, 024001
Alic D., Bona-Casas C., Bona C., Rezzolla L., Palenzuela C., 2012, Phys. Rev. D, 85, 064040
Alic D., Kastaun W., Rezzolla L., 2013, Phys. Rev. D, 88, 064049
Argast D., Samland M., Thielemann F.-K., Qian Y.-Z., 2004, A&A, 416, 997
Arlandini C., Käppeler F., Wisshak K., Gallino R., Lugaro M., Busso M., Straniero O., 1999, ApJ, 525, 886
Aso Y., Michimura Y., Somiya K., Ando M., Miyakawa O., Sekiguchi T., Tatsumi D., Yamamoto H., 2013, Phys. Rev. D, 88, 043007
Baiotti L., Rezzolla L., 2006, Phys. Rev. Lett., 97, 141101
Baiotti L., Giacomazzo B., Rezzolla L., 2008, Phys. Rev. D, 78, 084033
Baiotti L., Giacomazzo B., Rezzolla L., 2009, Class. Quantum Gravity, 26, 114005
Baiotti L., Shibata M., Yamamoto T., 2010, Phys. Rev. D, 82, 064015
Barnes J., Kasen D., 2013, ApJ, 775, 18
Baumgarte T. W., Shapiro S. L., 1999, Phys. Rev. D, 59, 024007
Baumgarte T. W., Shapiro S. L., Shibata M., 2000, ApJ, 528, L29
Bauswein A., Goriely S., Janka H.-T., 2013, ApJ, 773, 78
Berger E., 2014, ARA&A, 52, 43
Berger E. et al., 2005, Nature, 438, 988
Berger E., Fong W., Chornock R., 2013, ApJ, 774, L23
Bernuzzi S., Hilditch D., 2010, Phys. Rev. D, 81, 084003

Bernuzzi S., Thierfelder M., Brügmann B., 2012, Phys. Rev. D, 85, 104030
Brown D., Diener P., Sarbach O., Schnetter E., Tiglio M., 2009, Phys. Rev. D, 79, 044023
Ciolfi R., Siegel D. M., 2015, ApJ, 798, L36
Damour T., Guercilena F., Hinder I., Hopper S., Nagar A., Rezzolla L., 2014, Phys. Rev. D, 89, 081503
Dessart L., Ott C. D., Burrows A., Rosswog S., Livne E., 2009, ApJ, 690, 1681
Dietrich T., Moldenhauer N., Johnson-McDaniel N. K., Bernuzzi S., Markakis C. M., Bruegmann B., Tichy W., 2015, Phys. Rev. D, 92, 124007
East W. E., Pretorius F., 2012, ApJ, 760, L4
East W. E., Pretorius F., Stephens B. C., 2012a, Phys. Rev. D, 85, 124009
East W. E., Ramazanoğlu F. M., Pretorius F., 2012b, Phys. Rev. D, 86, 104053
East W. E., Paschalidis V., Pretorius F., 2015, ApJ, 807, L3
East W. E., Paschalidis V., Pretorius F., Shapiro S. L., 2016, Phys. Rev. D, 93, 024011
Eichler D., Livio M., Piran T., Schramm D. N., 1989, Nature, 340, 126
Einfeldt B., 1988, SIAM Journal on Numerical Analysis, 25, 294
Fernández R., Metzger B. D., 2013, MNRAS, 435, 502
Fernández R., Kasen D., Metzger B. D., Quataert E., 2015a, MNRAS, 446, 750
Fernández R., Quataert E., Schwab J., Kasen D., Rosswog S., 2015b, MNRAS, 449, 390
Fischer T., Whitehouse S. C., Mezzacappa A., Thielemann F.-K., Liebendörfer M., 2010, A&A, 517, A80
Fischer T., Hempel M., Sagert I., Suwa Y., Schaffner-Bielich J., 2014, Eur. Phys. J. A, 50, 46
Foucart F. et al., 2014, Phys. Rev. D, 90, 024026
Foucart F. et al., 2015, Phys. Rev. D, 91, 124021
Foucart F. et al., 2016, Phys. Rev., D93, 044019
Freiburghaus C., Rosswog S., Thielemann F.-K., 1999, ApJ, 525, L121
Galeazzi F., Kastaun W., Rezzolla L., Font J. A., 2013, Phys. Rev. D, 88, 064009
Gold R., Bernuzzi S., Thierfelder M., Brügmann B., Pretorius F., 2012, Phys. Rev. D, 86, 121501
Goodale T., Allen G., Lanfermann G., Massó J., Radke T., Seidel E., Shalf J., 2003, Vector and Parallel Processing – VECPAR'2002, 5th Int. Conf., Lecture Notes in Computer Science. Springer-Verlag, Berlin
Goriely S., Bauswein A., Just O., Pllumbi E., Janka H.-T., 2015, MNRAS, 452, 3894
Gourgoulhon E., Grandclement P., Taniguchi K., Marck J.-A., Bonazzola S., 2001, Phys. Rev. D, 63, 064029
Grossman D., Korobkin O., Rosswog S., Piran T., 2014, MNRAS, 439, 757
Hilditch D., Bernuzzi S., Thierfelder M., Cao Z., Tichy W., Brügmann B., 2013, Phys. Rev. D, 88, 084057
Hotokezaka K., Kiuchi K., Kyutoku K., Okawa H., Sekiguchi Y.-i., Shibata M., Taniguchi K., 2013, Phys. Rev. D, 87, 024001
Hotokezaka K., Piran T., Paul M., 2015, Nat. Phys., 11, 1042
Hüdepohl L., Müller B., Janka H.-T., Marek A., Raffelt G. G., 2010, Phys. Rev. Lett., 104, 251101
Ishimaru Y., Wanajo S., Prantzos N., 2015, ApJ, 804, L35
Ji A. P., Frebel A., Chiti A., Simon J. D., 2016, Nature, 531, 610
Just O., Bauswein A., Pulpillo R. A., Goriely S., Janka H.-T., 2015, MNRAS, 448, 541
Just O., Obergaulinger M., Janka H.-T., Bauswein A., Schwarz N., 2016, ApJ, 816, L30
Kaplan J. D., Ott C. D., O'Connor E. P., Kiuchi K., Roberts L., Duez M., 2014, ApJ, 790, 19
Kasen D., Badnell N. R., Barnes J., 2013, ApJ, 774, 25
Kasen D., Fernández R., Metzger B. D., 2015, MNRAS, 450, 1777
Kastaun W., Galeazzi F., 2015, Phys. Rev. D, 91, 064027
Kastaun W., Galeazzi F., Alic D., Rezzolla L., Font J. A., 2013, Phys. Rev. D, 88, 021501
Kiuchi K., Sekiguchi Y., Kyutoku K., Shibata M., Taniguchi K., Wada T., 2015a, Phys. Rev. D, 92, 064034
Kiuchi K., Cerdá-Durán P., Kyutoku K., Sekiguchi Y., Shibata M., 2015b, Phys. Rev. D, 92, 124034
Korobkin O., Rosswog S., Arcones A., Winteler C., 2012, MNRAS, 426, 1940
Kulkarni S. R., 2005, preprint (astro-ph/0510256)
Kyutoku K., Ioka K., Okawa H., Shibata M., Taniguchi K., 2015, Phys. Rev. D, 92, 044028
Lattimer J. M., Schramm D. N., 1974, ApJ, 192, L145
Lattimer J. M., Swesty D. F., 1991, Nucl. Phys. A, 535, 331
Lee W. H., Ramirez-Ruiz E., van de Ven G., 2010, ApJ, 720, 953
Liebendörfer M., Whitehouse S. C., Fischer T., 2009, ApJ, 698, 1174
LIGO Scientific Collaboration et al., 2015, Class. Quantum Gravity, 32, 074001
Li L.-X., Paczynski B., 1998, ApJ, 507, L59
Lindquist R. W., 1966, Ann. Phys., 37, 487
Lippuner J., Roberts L. F., 2015, ApJ, 815, 82
Löffler F. et al., 2012, Class. Quantum Gravity, 29, 115001
Margalit B., Piran T., 2015, MNRAS, 452, 3419
Martin D., Perego A., Arcones A., Thielemann F.-K., Korobkin O., Rosswog S., 2015, ApJ, 813, 2
Metzger B. D., Berger E., 2012, ApJ, 746, 48
Metzger B. D., Fernández R., 2014, MNRAS, 441, 3444
Metzger B. D. et al., 2010, MNRAS, 406, 2650
Metzger B. D., Bauswein A., Goriely S., Kasen D., 2015, MNRAS, 446, 1115
Meyer B. S., 1989, ApJ, 343, 254
Moldenhauer N., Markakis C. M., Johnson-McDaniel N. K., Tichy W., Brügmann B., 2014, Phys. Rev. D, 90, 084043
Murphy B. W., Cohn H. N., Lugger P. M., 2011, ApJ, 732, 67
Nakamura T., Oohara K., Kojima Y., 1987, Prog. Theor. Phys. Suppl., 90, 1
Nakar E., 2007, Phys. Rept., 442, 166
Nakar E., Piran T., 2011, Nature, 478, 82
Neilsen D., Liebling S. L., Anderson M., Lehner L., O'Connor E., Palenzuela C., 2014, Phys. Rev. D, 89, 104029
Nissanke S., Kasliwal M., Georgieva A., 2013, ApJ, 767, 124
O'Connor E., Ott C. D., 2010, Class. Quantum Gravity, 27, 114103
Obergaulinger M., Aloy M. A., Müller E., 2010, A&A, 515, A30
Oppenheimer J. R., Volkoff G. M., 1939, Phys. Rev., 55, 374
Palenzuela C., Liebling S. L., Neilsen D., Lehner L., Caballero O. L., O'Connor E., Anderson M., 2015, Phys. Rev. D, 92, 044045
Paschalidis V., East W. E., Pretorius F., Shapiro S. L., 2015, Phys. Rev. D, 92, 121502
Perego A., Cabezón R., Käppeli R., 2016, ApJS, 223, 22
Piran T., Nakar E., Rosswog S., 2013, MNRAS, 430, 2121
Plewa T., Müller E., 1999, A&A, 342, 179
Qian Y.-Z., 2000, ApJ, 534, L67
Radice D., Rezzolla L., 2013, ApJ, 766, L10
Radice D., Rezzolla L., Galeazzi F., 2014a, Class. Quantum Gravity, 31, 075012
Radice D., Rezzolla L., Galeazzi F., 2014b, MNRAS, 437, L46
Radice D., Rezzolla L., Galeazzi F., 2015, ASP Conf. Ser., 498, 121
Ramirez-Ruiz E., Trenti M., MacLeod M., Roberts L. F., Lee W. H., Saladino-Rosas M. I., 2015, ApJ, 802, L22
Rezzolla L., Kumar P., 2015, ApJ, 802, 95
Rezzolla L., Zanotti O., 2013, Relativistic Hydrodynamics. Oxford Univ. Press, Oxford
Rezzolla L., Baiotti L., Giacomazzo B., Link D., Font J. A., 2010, Class. Quantum Gravity, 27, 114105
Roberts L. F., Woosley S. E., Hoffman R. D., 2010, ApJ, 722, 954
Roberts L. F., Kasen D., Lee W. H., Ramirez-Ruiz E., 2011, ApJ, 736, L21
Rosswog S., 2015, Int. J. Mod. Phys. D, 24, 30012
Rosswog S., Liebendörfer M., Thielemann F.-K., Davies M. B., Benz W., Piran T., 1999, A&A, 341, 499
Rosswog S., Ramirez-Ruiz E., Davies M. B., 2003, MNRAS, 345, 1077
Rosswog S., Piran T., Nakar E., 2013, MNRAS, 430, 2585
Rosswog S., Korobkin O., Arcones A., Thielemann F.-K., Piran T., 2014, MNRAS, 439, 744
Ruffert M., Janka H.-T., Schäfer G., 1996, A&A, 311, 532

Sathyaprakash B. S., Schutz B. F., 2009, Living Rev. Rel., 12, 2
Schnetter E., Haley S., Hawke I., 2004, Class. Quantum Gravity, 21, 1465
Sekiguchi Y., Kiuchi K., Kyutoku K., Shibata M., 2015, Phys. Rev. D, 91, 064059
Shen S., Cooke R. J., Ramirez-Ruiz E., Madau P., Mayer L., Guedes J., 2015, ApJ, 807, 115
Shibata M., Nakamura T., 1995, Phys. Rev. D, 52, 5428
Shibata M., Taniguchi K., 2006, Phys. Rev. D, 73, 064027
Shibata M., Kiuchi K., Sekiguchi Y., Suwa Y., 2011, Prog. Theor. Phys., 125, 1255
Siegel D. M., Ciolfi R., Rezzolla L., 2014, ApJ, 785, L6
Stephens B. C., East W. E., Pretorius F., 2011, ApJ, 737, L5
Suresh A., Huynh H. T., 1997, J. Comput. Phys., 136, 83
Tanaka M., Hotokezaka K., 2013, ApJ, 775, 113
Tanvir N. R., Levan A. J., Fruchter A. S., Hjorth J., Wiersema K., Tunnicliffe R., Postigo A. d. U., 2013, Nature, 500, 547
Thorne K. S., 1981, MNRAS, 194, 439
Tolman R. C., 1939, Phys. Rev., 55, 364
Tsang D., 2013, ApJ, 777, 103
van de Voort F., Quataert E., Hopkins P. F., Kereš D., Faucher-Giguère C.-A., 2015, MNRAS, 447, 140
van Riper K. A., Lattimer J. M., 1981, ApJ, 249, 270
Wallner A. et al., 2015, Nat. Commun., 6, 5956
Wanajo S., Sekiguchi Y., Nishimura N., Kiuchi K., Kyutoku K., Shibata M., 2014, ApJ, 789, L39
Weyhausen A., Bernuzzi S., Hilditch D., 2012, Phys. Rev. D, 85, 024038
Zrake J., MacFadyen A. I., 2013, ApJ, 769, L29

APPENDIX A: NEUTRINO TRANSPORT DETAILS

A1 The Boltzmann equation for free-streaming neutrinos

We treat neutrinos as massless particles with four-momentum p^α, interacting with a (fluid) medium having four-velocity u^α. Following Thorne (1981), we decompose p^α as

$$p^\alpha = (-p_\beta u^\beta)(u^\alpha + r^\alpha)\,, \tag{A1}$$

where $E_\nu = -p_\alpha u^\alpha$ is the neutrino energy as measured by an observer comoving with the fluid and r^α is a unit spacelike four-vector orthogonal to the fluid four-velocity, i.e. such that

$$r_\alpha r^\alpha = 1\,,\quad u_\alpha r^\alpha = 0\,. \tag{A2}$$

From a more physical point of view, r^α represents the spatial direction of propagation of the neutrinos as seen by an observer comoving with the fluid. Finally, we introduce the four-propagation vector of the neutrinos

$$k^\alpha = u^\alpha + r^\alpha\,. \tag{A3}$$

Note that $k_\alpha k^\alpha = 0$.

The worldlines of neutrinos can be parametrized with the affine parameter

$$\ell = \int (-p_\alpha u^\alpha)\mathrm{d}s\,, \tag{A4}$$

so that

$$\left(\frac{\partial}{\partial \ell}\right)^\alpha = k^\alpha\,. \tag{A5}$$

Using ℓ, the Boltzmann equation for neutrino radiation transport can be written as (Thorne 1981)

$$\frac{DF}{D\ell} = \mathbb{C}[F]\,, \tag{A6}$$

where F is the distribution function of either electron or anti-electron neutrinos and $\mathbb{C}$ describes the interaction between neutrinos and the background fluid term *in the fluid frame*. Finally, $D/D\ell$ is the total derivative in phase-space along p^α:

$$\frac{DF}{D\ell} = k^\alpha\left[\frac{\partial F}{\partial x^\alpha} - \Gamma^\delta_{\alpha\beta}p^\beta\frac{\partial F}{\partial p^\delta}\right], \tag{A7}$$

where $\Gamma^\delta_{\alpha\beta}$ are the Christoffel symbols.

A2 Neutrino number density evolution

Following an approach similar to that of Liebendörfer, Whitehouse & Fischer (2009), we decompose neutrinos into a trapped component, which we treat with the leakage prescription, and a free-streaming component, which we evolve using a moment scheme. Our neutrino transport scheme evolves two equations describing the streaming of neutrinos along radial rays and their average energy evolution.

It is easily seen that the free-streaming neutrino distribution function also obeys the Boltzmann equation (A6), with an appropriate collisional term. In the simulations presented here, this term is approximated neglecting scattering of the free-streaming component of the neutrino radiation and using the effective emissivity from the leakage scheme to compute neutrino sources. Finally, the absorption opacities of electron neutrinos and anti-neutrinos are computed in the local thermodynamical equilibrium approximation, as in our leakage scheme.

We introduce the neutrino number current for a given neutrino flavor X (Lindquist 1966)

$$J^\alpha_{_X} = \int F p^\alpha \frac{\mathrm{d}^3 p}{-p_0}\,. \tag{A8}$$

$J^\alpha_{_X}$ is such that $n_{_X} = -u_\alpha J^\alpha_{_X}$ is the neutrino number density in the fluid rest frame. Neglecting scattering, the balance of absorption and emission of the free-streaming neutrinos can be derived from the first moment of the Boltzmann equation (Thorne 1981; Shibata et al. 2011),

$$\nabla_\alpha J^\alpha_{_X} = R^{\mathrm{eff}}_{_X} - \kappa_{_X} n_{_X}\,. \tag{A9}$$

In the previous equation, $R^{\mathrm{eff}}_{_X}$ is the effective neutrino emission rate, while $\kappa_{_X}$ is the absorption opacity.

Note that equation (A9) is exact but not closed. In order to solve it, it is necessary to construct a closure. In our simulations we close the equations assuming that neutrinos are streaming radially at the speed of light. This assumption is justified by the fact that we are only treating the free-streaming neutrinos.

Mathematically, this is equivalent to assuming

$$J^\alpha_{_X} = n_{_X} k^\alpha, \tag{A10}$$

where k^α is a fiducial null vector, which we construct from equation (A3) by taking r^α to be a radial unit-vector orthogonal to the fluid four-velocity u^α. This means that we are assuming the free-streaming neutrinos to be streaming radially in a frame instantaneously comoving with the fluid.

Under this assumption, we can derive a balance equation for $n_{_X}$

$$\partial_t(\sqrt{-g}n_{_X}k^t) + \partial_r(\sqrt{-g}n_{_X}k^r) = \sqrt{-g}\left(R^{\mathrm{eff}}_{_X} - \kappa_{_X}n_{_X}\right), \tag{A11}$$

where g is the determinant of the 4-metric (in spherical coordinates).

During the post-merger evolution, we solve equation (A11) on a series of independent radial rays using a first order, fully-implicit finite volume method. To handle the coupling with the hydrodynamics, we interpolate quantities interpolated from/to our standard

Cartesian AMR grid every timestep. For the results presented here, we used 2048 radial rays uniformly spaced in latitude and longitude and a radial resolution $\Delta r \simeq 244$ m.

A3 Neutrino average energy evolution

Since we are interested in modelling both composition and temperature changes due to neutrino absorption, a way to compute the average neutrino energy is also needed. For this purpose, we evolve the average (free-streaming) neutrino energies under the approximation of stationary spacetime, that is we assume that $t^\alpha := (\partial_t)^\alpha$ is a Killing vector. Under this assumption the quantity $(-p_\alpha t^\alpha)$ is conserved along neutrino worldlines in absence of interactions with the fluid:

$$\frac{\mathrm{d}(-p_\alpha t^\alpha)}{\mathrm{d}\ell} = 0\,. \tag{A12}$$

The quantity $\mathcal{E}_X = -p_\alpha t^\alpha$ is the energy of neutrinos of flavor X as seen by the 'coordinate observer' (a non-physical observer with four-velocity t^α). In particular

$$\mathcal{E}_X = -p_\alpha t^\alpha = -E_X k_\alpha t^\alpha =: E_X \chi\,. \tag{A13}$$

Within this approximation, we can write an equation for the average neutrino energy

$$\frac{\mathrm{d}\mathcal{E}_X}{\mathrm{d}\ell} = \frac{R^{\mathrm{eff}}_X}{n_X}\left(\chi\,\frac{Q^{\mathrm{eff}}_X}{R^{\mathrm{eff}}_X} - \mathcal{E}_X\right), \tag{A14}$$

where Q^{eff}_X is the effective neutrino energy source (which we again take from the leakage scheme). Assuming radial propagation, equation (A14) can be rewritten as

$$n_X k^t \partial_t \mathcal{E}_X + n_X k^r \partial_r \mathcal{E}_X = \left(\chi\, Q^{\mathrm{eff}}_X - \mathcal{E}_X R^{\mathrm{eff}}_X\right). \tag{A15}$$

This equation is solved on the same grid as equation (A11) using a fully implicit upwind first order finite-differencing method.

APPENDIX B: COUPLING BETWEEN HYDRODYNAMICS AND NEUTRINOS

Equations (3) and (5) are solved using an operator split approach. We use a standard 1st order explicit time update to treat the momentum deposition by neutrinos. However, to avoid issues with the heating/cooling and composition sources becoming stiff, we use a semi-implicit update formula for the evolution of the conserved energy and proton-number densities.

In the context of the operator split method, we need to update energy and number densities by solving equations of the form

$$\frac{\mathrm{d}u}{\mathrm{d}t} = f\,, \tag{B1}$$

over a single time step. In equation (B1), f is possibly large, while u is a positive quantity (being a number or energy density), which we wish to maintain positive during the evolution. Note that in our EOS implementation we include all binding energy contributions to the energy density in the definition of m_b. In this way the specific internal energy per baryon and the evolved energy density are always positive quantities. Possibly problematic cases are regions with strong cooling (i.e. $f \ll 0$ and $u < |f|\Delta t$) or small proton fractions.

To update u while keeping it positive in these cases, we define the quantity $\theta = f/u$ and update u using the following semi-implicit scheme

$$\frac{u^{k+1} - u^k}{\Delta t} = \theta^k u^{k+1}\,. \tag{B2}$$

In the previous equation, the superscript k denotes a function at time $t = k\Delta t$. It is easy to see that equation (B2) implies

$$u^{k+1} = \frac{u^k}{1 - \theta^k \Delta t}\,, \tag{B3}$$

which manifestly ensures positivity of the solution (note that θ is negative in the problematic cases).

This paper has been typeset from a TEX/LATEX file prepared by the author.